

ARTICLE OPEN



Australia's Black Summer pyrocumulonimbus super outbreak reveals potential for increasingly extreme stratospheric smoke events

David A. Peterson¹✉, Michael D. Fromm², Richard H. D. McRae³, James R. Campbell¹, Edward J. Hyer¹, Ghassan Taha^{4,5}, Christopher P. Camacho¹, George P. Kablick III⁶, Chris C. Schmidt⁶ and Matthew T. DeLand⁷

The Black Summer fire season of 2019–2020 in southeastern Australia contributed to an intense ‘super outbreak’ of fire-induced and smoke-infused thunderstorms, known as pyrocumulonimbus (pyroCb). More than half of the 38 observed pyroCbs injected smoke particles directly into the stratosphere, producing two of the three largest smoke plumes observed at such altitudes to date. Over the course of 3 months, these plumes encircled a large swath of the Southern Hemisphere while continuing to rise, in a manner consistent with existing nuclear winter theory. We connect cause and effect of this event by quantifying the fire characteristics, fuel consumption, and meteorology contributing to the pyroCb spatiotemporal evolution. Emphasis is placed on the unusually long duration of sustained pyroCb activity and anomalous persistence during nighttime hours. The ensuing stratospheric smoke plumes are compared with plumes injected by significant volcanic eruptions over the last decade. As the second record-setting stratospheric pyroCb event in the last 4 years, the Australian super outbreak offers new clues on the potential scale and intensity of this increasingly extreme fire-weather phenomenon in a warming climate.

npj Climate and Atmospheric Science (2021)4:38; <https://doi.org/10.1038/s41612-021-00192-9>

INTRODUCTION

An intense, multi-day outbreak of fire-induced and smoke-infused thunderstorms (known as pyrocumulonimbus or pyroCb) occurred during 29–31 December 2019 and 04 January 2020 in southeastern Australia. This Australian New Year Super Outbreak (ANYSO) of pyroCb activity resulted in roughly 1.0 Tg of cumulative smoke particle mass being injected into the lower stratosphere¹, consistent in magnitude with the initial ash and sulfate plume of a moderate volcanic eruption². ANYSO was part of Australia's extreme Black Summer³, which featured many catastrophic bushfires that burned a record 7.4 million hectares of land⁴, an area slightly smaller than the Czech Republic. ANYSO occurred within three years of the Pacific Northwest Event (PNE) in western North America (12 August 2017), which served as the previous benchmark for an extreme, lower-stratospheric pyroCb smoke mass injection (albeit three times smaller). The PNE inspired a diverse set of recent studies aimed at understanding fundamental pyroCb smoke plume processes and feedbacks in the lower stratosphere^{1,2,5–8}. ANYSO has raised the bar significantly in terms of intensity and scale. Dramatic shifts in stratospheric composition, radiative balance, and even regional circulation now appear possible from extreme pyroCb events. Given the prospects of continuing climate change, and the increasing intensity of severe fire seasons globally^{9,10}, pyroCb research is entering a new phase focused on reconciling larger scales of potential atmospheric impacts and climate feedbacks.

When compared with typical convective storms, pyroCbs are characterized by relatively smaller cloud droplet and ice particle size distributions, caused by an overabundance of smoke particles that dominate nucleation, condensation, and freezing processes¹¹. Smaller inherent size distributions within the inner storm core

suppress precipitation^{12–14}, which inhibits scavenging and redistribution of smoke downward toward the ground. A considerable quantity of smoke particle mass is therefore exhausted from the top of pyroCbs through the high-altitude anvil outflow region, forming an efficient vertical smoke-transport pathway¹⁵. PyroCb activity is often characterized by extreme updraft velocities (up to 35 to 58 m s^{−1})^{16,17} that rapidly transport smoke particles directly from the surface to the lower stratosphere, similar to an explosive volcanic eruption².

PyroCb activity was first recognized in 2000 and 2003^{18,19}, and has only been routinely monitored and inventoried using the satellite remote sensing advances of the last decade²⁰. Scientific and public interest has grown rapidly in response, as destructive fire seasons in recent years have increasingly featured intense pyroCb activity^{2,20–22}. These unusual storms are driven by a common meteorology, requiring dry air near the surface to nurture vigorous fire activity, and a complementary moisture source several kilometers aloft to facilitate condensation, latent heat release, and subsequent enhancement to the buoyancy of growing convective cells^{21,23–25}. PyroCb development typically occurs during local afternoon and evening, when diurnal cycles of surface temperature, fire sensible heating, and atmospheric instability reach their maximums²². The synergy of favorable meteorology with broad and vigorous wildfire episodes generally limits pyroCb development to active summertime fire seasons in Australia, North America, and northern Asia^{20,22,26–28}. The climatological occurrence of favorable conditions likely explains why pyroCb activity is endemic and far more frequent than volcanic eruptions worldwide.

PyroCb smoke plumes reaching the lower stratosphere often result from multiple large wildfires in close proximity that produce

¹Naval Research Laboratory, Monterey, CA, USA. ²Naval Research Laboratory, Washington, DC, USA. ³ACT Emergency Services Agency, Canberra, Australia. ⁴Universities Space Research Association (USRA), Greenbelt, MD, USA. ⁵NASA – Goddard Space Flight Center, Greenbelt, MD, USA. ⁶University of Wisconsin–Madison, Madison, WI, USA. ⁷Science Systems and Applications, Inc. (SSAI), Lanham, MD, USA. ✉email: david.peterson@nrlmry.navy.mil

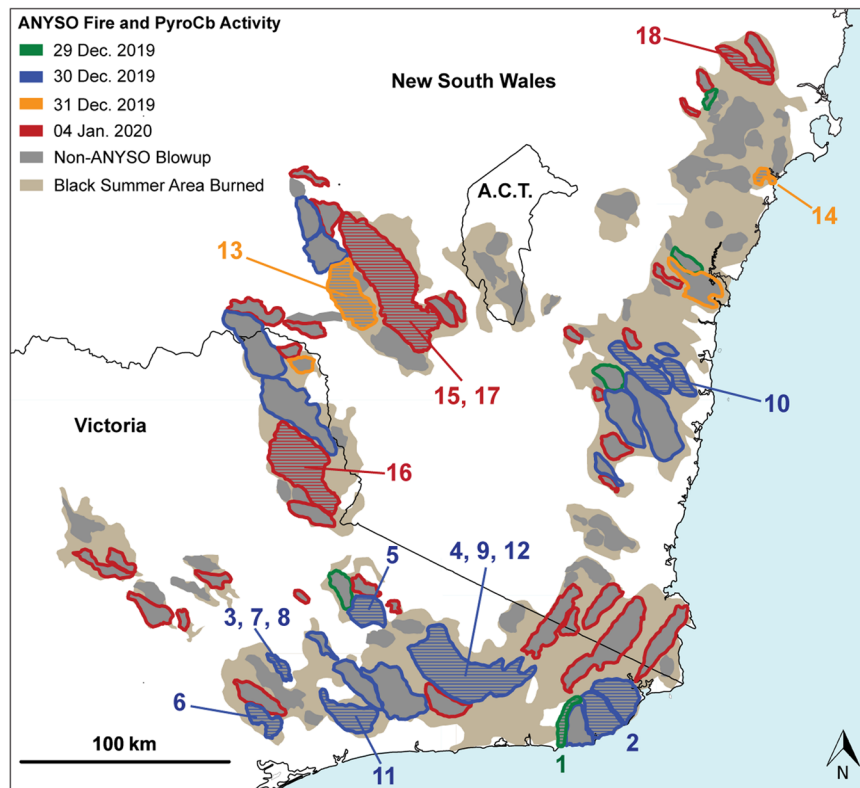


Fig. 1 Map of the blow-up fires contributing to ANYSO pyroCb activity. Light brown shading shows the full area burned during the ‘Black Summer’ fire season of 2019–2020, with 109 individual blow-up fires superimposed in dark grey. Perimeters of blow-up fires during the ANYSO period are color-coded by date. Hatching in the same color scheme identifies the 13 blow-up fires that contributed to pyroCb development. Numbers identify the approximate initiation points of 18 pyroCb sub-events, corresponding with the ANYSO timeline in Fig. 4.

several intense convective updrafts over a period of only a few hours^{2,27}. PyroCb intensity and ensuing stratospheric plume impacts therefore vary with the distribution and intensity of certain types of regional wildfire activity during periods that overlap with conditions that include conducive background meteorology. While regionally-focused pyroCb outbreaks deviate from single point sources associated with volcanic eruptions, the ensuing smoke plumes exhibit many similarities, traveling thousands of kilometers in both the upper troposphere and lower stratosphere (UTLS), even encircling a portion of the globe^{1,2,29,30}.

Smoke plumes ensuing from ANYSO reached extraordinary altitudes in the middle stratosphere (20–35 km)¹, where the absorption of incoming sunlight by carbonaceous smoke particles can perturb radiative forcing⁷ and facilitate photochemical reactions that influence ozone chemistry⁸. ANYSO also revealed that plumes injected by pyroCb activity can significantly alter the dynamic circulation in the lower stratosphere^{1,30,31}. This discovery raises many new questions on the scale and impact of pyroCb activity in the climate system at a time when stratospheric geoengineering is being evaluated as a response to climate change³² and tropospheric smoke sources are often omitted from reviews of the lower-stratospheric aerosol system^{33,34}.

Are the recent PNE and ANYSO harbingers of even larger pyroCb outbreaks capable of rivaling the aerosol mass injection magnitude of major volcanic eruptions^{35,36}, such as the 1991 Pinatubo eruption? Is the potential for pyroCb super outbreaks increasing in a warming climate? Could a series of large pyroCb outbreaks rival the potential climate impacts expected following a nuclear war^{8,37}? Observations of the recent ANYSO provide important clues to these now relevant and pressing questions. By examining the many remarkable features of ANYSO, this study identifies and characterizes important indicators of extremely

large smoke plumes ensuing from regional outbreaks of sustained pyroCb activity. A variety of satellite, weather radar, and meteorological measurements are employed, with a focus on understanding distinct pyroCb and wildfire characteristics that differed from both the PNE and prior canonical pyroCb analyses. Specifically, we focus on the unusually long duration of ANYSO, anomalously intense nocturnal pyroCb activity, and evolution of the ensuing smoke plumes in the stratosphere. This analysis provides critical perspective on the mechanics driving extreme pyroCb outbreaks and their potential interactions with a warming climate.

RESULTS

ANYSO in perspective

ANYSO is characterized here as a pyroCb ‘super outbreak’ because of its exceptional scale and magnitude relative to historical precedent^{2,29,38,39}. It featured an unusually large number of distinct, ice-capped convective columns (38 total), known as pyroCb ‘pulses’, over a prolonged period (51 non-consecutive hours). Each pyroCb pulse developed over a subset of particularly intense wildfires, or ‘blow-up fires’, defined by rapid increases in rate of fire spread and intensity (see Methods section), as well as significant vertical smoke plume growth that extends above the planetary boundary layer^{40–43}.

Figure 1 (dark gray shading) depicts the expansive regions burned by 109 individual blow-up fires documented during the peak of the Black Summer fire season (25 Nov. 2019 to 4 Feb. 2020) across the states of Victoria and New South Wales, and the Australian Capital Territory (ACT). Four of these blow-up fires contributed to what was a relatively small pyroCb event on 21 December 2019. The subsequent and larger ANYSO that began on

29 December was driven by 13 blow-up fires, which are shaded by date of occurrence and numbered sequentially based on time of pyroCb development (UTC). The total area burnt by the ANYSO blow-up fires was estimated at 530,000 ha, or slightly larger than the state of Delaware (land area) in the United States. An energy release of $\sim 1.3\text{--}5.1 \times 10^{11}$ MJ was estimated for this subset of fires, which is equivalent to $32\text{--}127 \times 10^6$ tons of TNT or more than 2000 times the energy of the Hiroshima atomic explosion (see methods). While the fires driving the PNE burned in coniferous forest, with significant logging slash buildup⁴⁴, ANYSO burned primarily Eucalyptus forest. These forests are notorious for extremely rapid fire spread, reflecting eucalypt leaf litter buildup, shrub layer flammability, and dense spotting over a range of distances⁴⁵.

ANYSO occurred in two distinct phases, with the first and largest occurring during 29–31 December. This initial phase was significant for many reasons, but most notably for its overall duration of ~ 45 h (09:30 UTC, 29 December to 06:40 UTC, 31 December). Some of the most intense pyroCb activity occurred during nighttime, which deviates from established conceptual models for pyroCb growth^{21,22}. The first phase of ANYSO included 28 blow-up fires (Fig. 1, green, blue, orange), with 10 generating 33 distinct pyroCb pulses, all of which injected smoke into the UTLs. For comparison, the 2017 PNE², 2009 Black Saturday³⁸, and 2001 Chisholm pyroCb events^{29,39} each featured fewer than 10 pulses over a constrained period of <24 total hours, occurring almost exclusively during the local late-afternoon and evening.

The second phase of ANYSO commenced on 04 January 2020, after 3 days without pyroCb activity. It included more blow-up fires than the first phase (35 total), but only three generated pyroCb activity (Fig. 1, red), including five additional pulses. The duration of pyroCb activity was more typical of previous significant events, spanning just over six hours (03:00 to 9:10 UTC).

Figure 2a shows a true color satellite image (GeoColor) from the Advanced Baseline Imager onboard the GOES-17 satellite on 02 January 2020. It highlights the stratospheric smoke plume resulting from pyroCb activity during the first phase (ending on 31 December 2019), evidenced by dark smoke surmounting bright regions of cloud cover. Figure 2b provides a similar display for 07 January, highlighting the plume initiated by the second phase of pyroCb activity (04 January). The combination of radar and lidar data applied in this study reveals that both ANYSO plumes were injected directly into the lower stratosphere by earlier pyroCb activity. These plumes covered much of the South Pacific Ocean within 48–72 h of pyroCb cessation, similar to the continental-scale plume generated by the 2017 PNE² (Fig. 2c).

ANYSO's first phase now stands as the largest known stratospheric injection of smoke particles linked to a distinct period of pyroCb activity (0.2–0.8 Tg, Fig. 3). By itself, it was about a factor of two larger than the PNE and an order of magnitude larger than the 2001 Chisholm (0.01–0.1 Tg)²⁹ and 2009 Black Saturday events (0.05–0.1 Tg, see Methods section). The stratospheric plume was consistent in magnitude with the initial stages of a moderate-scale volcanic eruption. For instance, the Kasatochi eruption in Alaska (7–8 August 2008) injected an initial 0.2–0.5 Tg of ash and sulfate-based particles into the lower stratosphere². While the Kasatochi plume particle mass was at least an order of magnitude smaller than plumes associated with extreme volcanic eruptions, such as Pinatubo in 1991^{35,36}, the comparison is highly consistent with more frequent, but less explosive eruptions.

ANYSO's second phase injected an estimated 0.1–0.3 Tg of additional smoke particle mass into the lower stratosphere, which is consistent with that of the PNE (Fig. 3). The cumulative smoke particle mass injected into the stratosphere by both phases of pyroCb activity was 0.3–1.1 Tg (Fig. 3). This combined plume was at least three times larger than the PNE and likely exceeded the Kasatochi eruption. Comparisons with 'bottom-up' estimates of the mass of smoke particles released by the blow-up fires

(0.1–1.2 Tg) indicates that these 'bottom-up' estimates are either strongly underestimated using climatological/ecological mean values of fuel loading and consumption, or that emitted smoke particles are transported very efficiently to the stratosphere, or both (see Methods section).

PyroCb activity driving smoke transport to the stratosphere

To account for the complexity of ANYSO, the aforementioned 38 pyroCb pulses were divided into 18 distinct 'sub-events', defined as an individual pyroCb pulse or chain of several pulses anchored to one of the 13 blow-up fire initiation points. Figure 1 reveals that the majority of these blow-up fires produced a single pyroCb sub-event. However, three blow-up fires were linked to multiple sub-events, primarily during peak activity on 30 December. Figure 4 includes a detailed timeline of all 18 sub-events, with bars representing individual pulses. Each pulse was identified using thermal infrared ($11\text{ }\mu\text{m}$) brightness temperature (BT_{11}) imagery from the Advanced Himawari Imager (AHI) onboard the Himawari-8 satellite (see Methods section). Full animations of the fire and pyroCb activity observed by AHI during both ANYSO phases are provided in Supplementary Information. All times related to this analysis use UTC, which is 11 h behind the local time (LT) in Eastern Australia (00:00 UTC = 11:00 LT).

Regional C-band weather radar (5 cm wavelength) echo-top observations were incorporated to identify the approximate injection altitude of each pulse relative to the tropopause (see methods), revealing that 20 of the 38 pyroCb pulses (53%) reached the lower stratosphere. However, when considering that pyroCb echo-top observations can be underestimated by as much as one kilometer¹⁴, it is possible that several more pyroCb pulses actually reached that layer. The echo-tops from three pulses extended directly into the stratospheric overworld⁴⁶, coinciding with a potential temperature (θ) >380 K. PyroCb activity was especially intense during seven sub-events (Fig. 4, red boxes), characterized by the highest pyroCb echo-top altitudes and longest durations of echo-tops extending above the tropopause. This subset likely represents the largest stratospheric injections of smoke particles during ANYSO. Maximum radar echo-tops and θ values observed during each pyroCb sub-event are summarized in Supplementary Table 1.

The first phase of ANYSO began around sunset on 29 December near the coast of eastern Victoria. While several blow-up fires were observed on this date, only one contributed to pyroCb development, burning $\sim 32,500$ ha. The first of four pyroCb pulses (sub-event #1 in Figs. 1 and 4) developed at 09:30 UTC (20:30 LT), and the final pulse ended 8 h later near 18:40 UTC (05:40 LT). The full duration of this first sub-event occurred at night. BT_{11} imagery (Fig. 5a) highlights the extremely cold cloud tops ($BT_{11} = -64^\circ\text{C}$) of the third pyroCb pulse, suggesting a likely overshoot above the tropopause into the lower stratosphere. Radar echo-top observations confirm that this pyroCb pulse injected smoke particles at least 15 km ($\theta = 374$ K), which is 1.5 km above the tropopause (13.5 km).

The most extreme pyroCb activity observed during ANYSO occurred on 30 December. This was also the first known occurrence of continuous pyroCb activity over an entire 24 h period. Seven blow-up fires with associated pyroCb were observed, burning 202,000 ha. Eleven distinct pyroCb sub-events occurred in eastern Victoria and one in New South Wales (Fig. 1), ultimately producing 25 individual pulses (Fig. 4). At least 13 of these (52%) injected smoke into the lower stratosphere. Four of the 11 pyroCb sub-events (#2, 10, 11, and 12) were responsible for significant stratospheric smoke particle injections, with some of the largest occurring at night or during the local morning hours.

Sub-events #2 and #4 coincided with the first intense daytime pyroCb activity observed during the first phase of ANYSO. While relatively short-lived, two of the three pulses from sub-event #2,

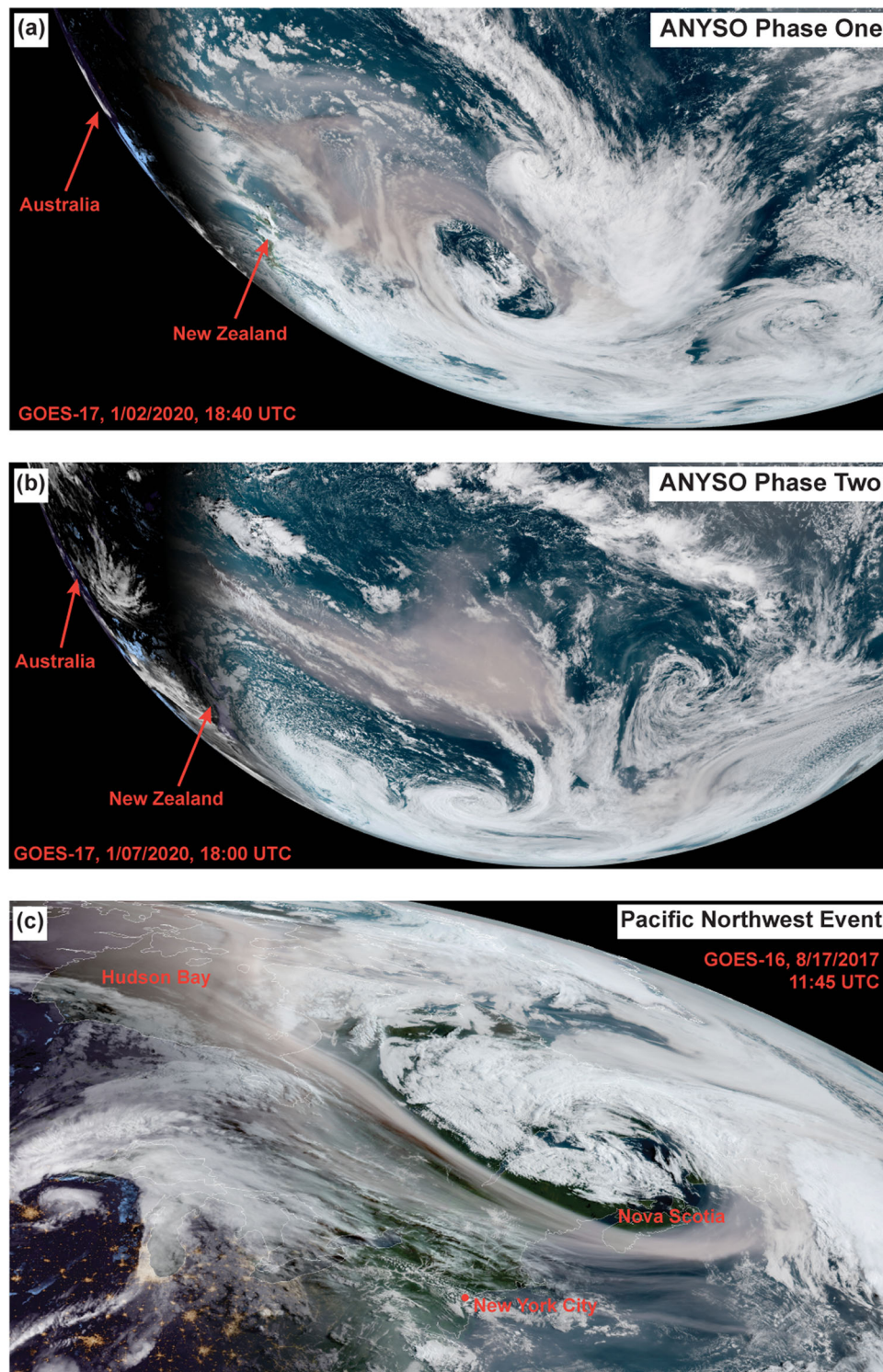


Fig. 2 The three largest pyroCb smoke plumes observed in the stratosphere to date. Each true color image is based on the GeoColor Algorithm (used with permission from the Cooperative Institute for Research in the Atmosphere) near local sunrise within 48–72 h of: **a** ANYSO phase one, **b** ANYSO phase two, and **c** the 2017 Pacific Northwest Event (PNE). The ANYSO images are from GOES-17. The PNE image (GOES-16) is adapted from our previous study².

injected smoke more than one kilometer above the tropopause (maximum of 16.3 km, $\theta = 397$ K). The third pulse of sub-event #4 persisted for more than 2 h, also injecting smoke above the tropopause. Figure 5b highlights the mature stage of this pulse, along with the remnants of sub-event #2 (second pulse) and other sub-events using an existing daytime algorithm²⁰ that

distinguishes the unique microphysics of pyroCb activity from traditional convective clouds (orange shading, see methods).

The combined anvil cloud from sub-events #11 and #12 (Fig. 5c) reached altitudes of at least 15.8 km ($BT_{11} < -70$ °C, $\theta = 392$ K), exceeding the tropopause by 2.3 km in the middle of the night on 30 December (~16:00 UTC, 03:00 LT). This likely marked

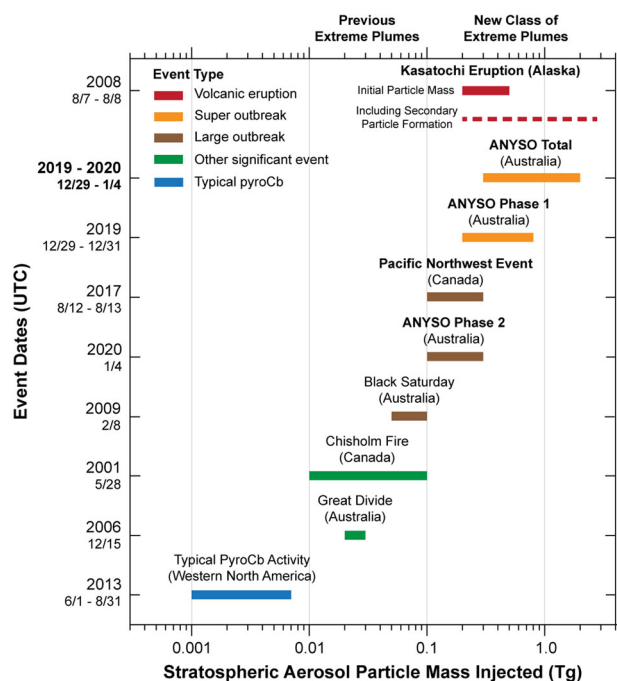


Fig. 3 ANYSO compared with stratospheric particle mass estimates from other events. Bars indicate the approximate uncertainty range of stratospheric aerosol particle mass injected. All mass estimates are displayed using a logarithmic scale (x-axis). Color scheme indicates event type and characteristics. This display expands upon an earlier version provided in our previous study².

the most extreme stratospheric smoke injection during the first phase of ANYSO. The New South Wales pyroCb sub-event (#10) generated six individual pulses over more than 11 h, which was the most of the 18 sub-events (Figs. 1 and 4). The fifth pulse, occurring during the local morning hours (31 December), was the largest (Fig. 5d), also signifying a significant stratospheric injection (14.7 km, $\theta = 371$ K). Two additional pyroCb sub-events developed on 31 December (Fig. 5e), supporting more than four hours of intermittent daytime pyroCb activity. While one of these sub-events (#13) produced three pulses, with one injecting into the stratosphere, radar, and satellite data suggest that the pyroCb activity this day did not significantly contribute to the stratospheric smoke plume from the first phase of ANYSO (Fig. 4).

The second phase of ANYSO occurred entirely on 04 January, primarily during local daytime and early evening. Three blow-up fires contributed to four pyroCb sub-events, with three occurring in New South Wales and one in Victoria (Fig. 1). The total area burned by these 04 January blow-up fires (245,000 ha) exceeded the total area burnt by the blow-up fires on 30 December (~202,000 ha). Five intermittent pyroCb pulses occurred over six hours (Fig. 4). Two pyroCb sub-events (#15 and #16) near the border between Victoria and New South Wales were extremely intense when observed near sunset (Fig. 5f), with echo-top altitudes reaching 16.4–16.7 km ($\theta = 375$ –390 K) and exceeding the tropopause (15.0 km) by 1.4–1.7 km. Both of these were comparable with the most intense pyroCb sub-events on 30 December (#11 and #12, $BT_{11} < -70$ °C, $\theta = 392$ K), each comprised of a single pulse that persisted for ~75 min. When considering that the other pyroCb pulses on 04 January did not significantly penetrate the tropopause, the majority of the stratospheric smoke particle mass injected during the second phase likely originated from these two pyroCb pulses alone.

Meteorology supporting a pyroCb super outbreak

The majority of extreme pyroCb events are driven by a distinct set of large-scale (synoptic) weather conditions^{21,23}, especially those resulting in the largest stratospheric smoke plumes (e.g., the 2017 PNE)². Analysis of synoptic meteorology is also a critical step in forecasting tornado super outbreaks^{47,48} and other severe weather events. Figure 6a, b reveals that both phases of ANYSO pyroCb activity developed as a strong anticyclonic circulation (high pressure) began to weaken, just ahead of an approaching cyclonic weather disturbance (low pressure trough) and its associated surface-based frontal boundary. While this synoptic weather pattern is well recognized for supporting extreme fire behavior^{49,50}, it also favors a deep, dry, and unstable near-surface mixed layer surmounted by a moisture source and decreased stability in the mid-troposphere. These thermodynamic conditions match a previously developed conceptual model for pyroCb activity²¹ that supports simultaneous development of extreme fire behavior at the surface and deep, moist convection (thunderstorms) aloft. The combination of approaching surface frontal boundaries and a relatively strong upper-level jet stream provided an additional dynamic forcing mechanism to enhance ascent in the troposphere. The tropopause altitude remained relatively uniform over the fires and pyroCb activity, within the warm air mass ahead of the frontal boundaries. A more detailed meteorological analysis for both ANYSO phases is provided in Supplementary Figs. 1–6.

The key distinguishing characteristic of ANYSO's first phase was the anomalous and persistent transport of moisture in the mid-troposphere over southeast Australia. Total precipitable water was more than 20 mm higher than the 30-year climatology over the blow-up fires in southeastern Australia near the peak of pyroCb activity (Fig. 6a). Transport of this moisture source was focused in the mid-troposphere along smaller weather disturbances within the unstable air mass preceding the primary cold front (Supplementary Figs. 1, 2, and 4). A series of these prefrontal troughs persisted over southeastern Australia from 06:00 UTC on 29 December until the primary frontal boundary cleared the region around 09:00 UTC on 31 December. Each prefrontal trough likely increased the potential for deep flaming, through hot, dry, and windy fire weather near the surface⁴³. Upper-level dynamics also became increasingly supportive of large-scale ascent in the region ahead of the primary cold front, evidenced by diverging winds at the jet stream altitude (250 hPa; Supplementary Fig. 3). The large number of blow-up fires (28 total) and unusually long duration of sustained pyroCb activity (~45 h) observed during ANYSO's first phase therefore resulted from a combination of favorable thermodynamic conditions and enhanced dynamic forcing that persisted over the fires in southeastern Australia within an expansive prefrontal environment.

The approaching synoptic weather disturbances sustained conditions suitable for extreme fire and pyroCb activity well after sunset^{23,27,38}, deviating from the typical diurnal cycle⁵¹. This is evidenced in a time series of hourly fire radiative power (FRP, units of MW, see methods) retrieved from AHI for all fire activity in southeast Australia (Fig. 6c). FRP provides information on the radiant heat output of fires detected from space and is commonly used as a proxy for fire intensity⁵². The display in Fig. 6c reveals that intense burning persisted during the entire duration of the first phase, both during local daytime and nighttime. As highlighted in Fig. 5c, the most intense blow-up fires and highest pyroCb echo-top altitudes (via sub-events #11 and #12) were observed over Victoria during the local nighttime period on 30 December, ahead of the cold front as it approached the active fires and associated FRP maximum. This nocturnal period also coincided with the strongest low-level winds speeds and largest burn rate by blow-up fires in the first phase, approaching

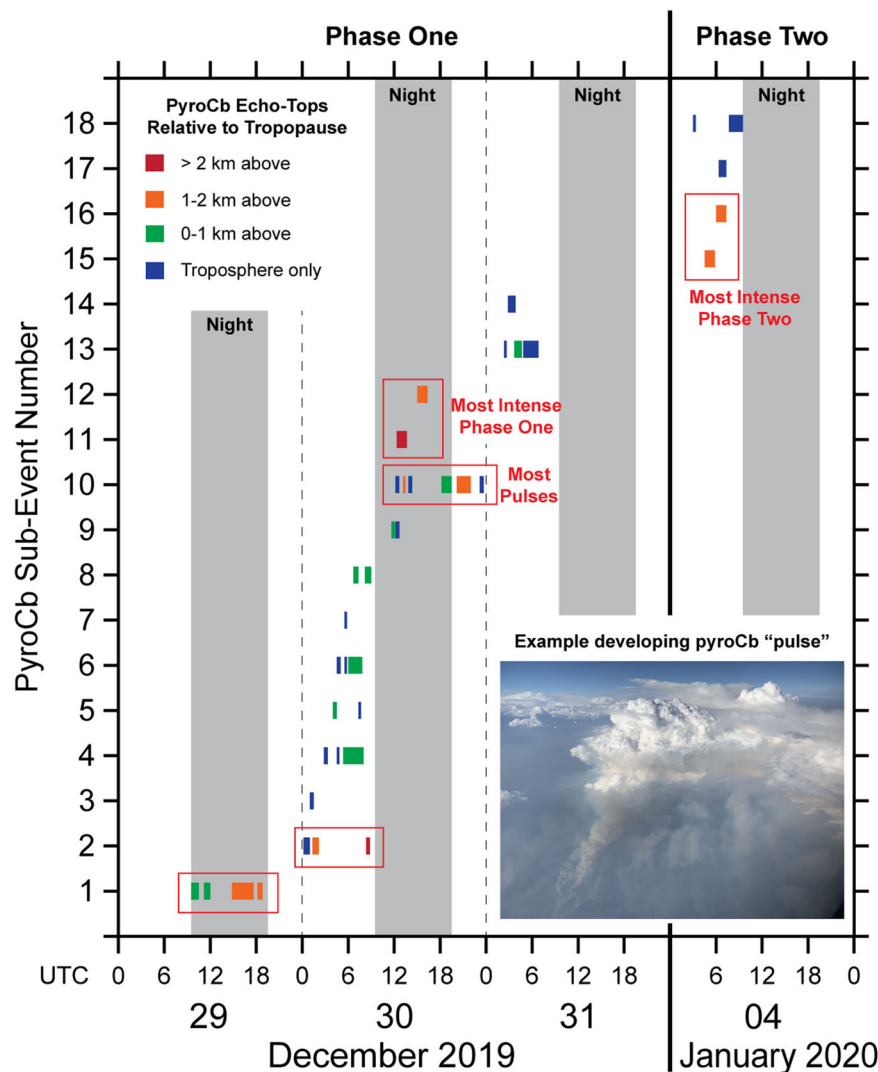


Fig. 4 Timeline of 18 pyroCb sub-events observed during ANYSO. Bars indicate 38 individual pyroCb pulses that injected smoke particles into the UTLS. Each bar includes all 10-min intervals that coincide with AHI BT₁₁ values below -35°C (pyroCb threshold) near each contributing blow-up (displayed in Fig. 1). Shading indicates the maximum radar echo-top altitude of each pulse relative to the tropopause altitude (13.5 km for phase one and 15.0 km for phase two), identifying the 20 pulses that injected smoke directly into lower stratosphere. PyroCb sub-events responsible for the largest stratospheric smoke injections are highlighted with red boxes. Inset picture shows an example pyroCb pulse in its developing stages (taken during the 2019 Fire Influence on Regional to Global Environments Experiment - Air Quality (FIREX-AQ)⁶⁹, D. Peterson).

100,000 ha per hour (~5.6 times the area of the District of Columbia, United States). In between the two ANYSO phases, meteorological conditions did not match the pyroCb conceptual model²¹, and no pyroCb activity was observed, despite continued burning and large FRP.

Synoptic meteorology during ANYSO's second phase was similar to the first (Supplementary Fig. 5). However, the local region along and ahead of the frontal boundary was narrower, featuring only one prefrontal trough. Less moisture was available in the mid-troposphere (Supplementary Fig. 6), with positive precipitable water anomalies peaking farther east (Fig. 6b). Only three out of thirty-five blow-up fires supported pyroCb activity (Fig. 1), despite coinciding with the largest area burned by blow-up fires and highest regional FRP values observed during the entire ANYSO period (Fig. 6c). Synoptic weather progression was also more rapid, which limited residence time in the relatively narrow prefrontal environment, thereby constraining pyroCb activity to approximately six hours.

Rapidly evolving synoptic weather features were a key factor limiting the duration of significant pyroCb outbreaks prior to ANYSO, including Black Saturday³⁸, Chisholm¹¹, and the PNE². It is possible that these events would have reached a magnitude similar to ANYSO under more persistent synoptic weather patterns. This is especially true for the PNE, given the large number of active wildfires observed in western Canada during 2017⁵³. Similarly, the western United States did not experience a pyroCb outbreak like ANYSO during the recent 2020 fire season, despite coinciding with a record number of large wildfires and several pyroCb events^{54–56}. In this case, few large weather disturbances were observed to nurture pyroCb development. Future pyroCb super outbreaks will occur similarly in favored regions at the confluence of large wildfires and favorable meteorology, especially when the critical transition period between transient disturbances persists for more than 24 h. This is the primary attribute that must be characterized and monitored as regional climate conditions continue evolving, particularly with

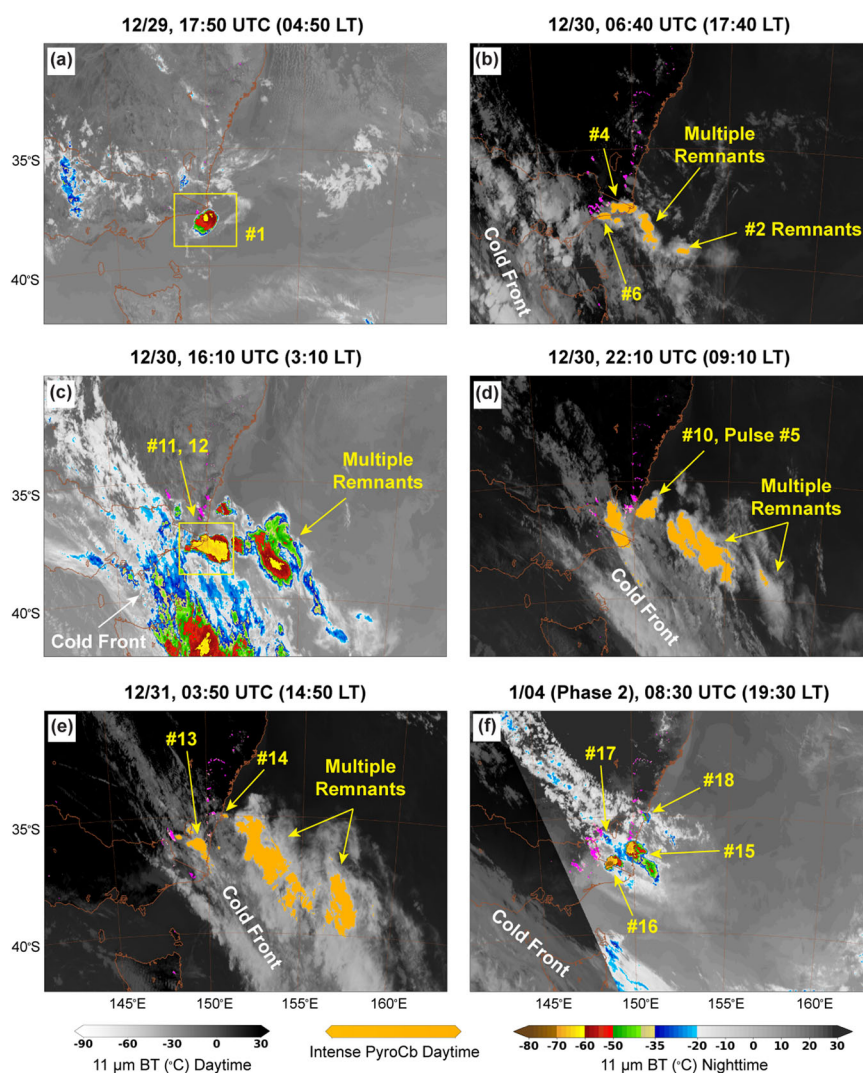


Fig. 5 Key stages of ANYSO pyroCb activity observed from satellite. Grayscale shading indicates daytime BT₁₁ from AHI, with colder, high-altitude cloud tops displayed in white. Orange shading coincides with smoke-perturbed pyroCb cloud tops. Multi-color shading indicates nighttime BT₁₁, with high-altitude cloud tops displayed in red, yellow, and brown (e.g., #16). PyroCb sub-event numbers match those in Figs. 1 and 4, with **a–e** highlighting sub-events observed during ANYSO's first phase and **f** highlighting peak activity during phase two. AHI pixels with active fires are displayed in pink. The approximate position of an approaching surface cold front is denoted in white. Animations of this imagery are provided in Supplementary Information for both ANYSO phases.

regards to the propensity of increasing scales of pyroCb intensity and stratospheric impact.

Smaller-scale meteorology also plays a significant role during pyroCb outbreaks, including specific forms of surface fire spread induced by the interaction of localized wind patterns with fuels and topography^{28,43}. Potential feedbacks induced by radiative heating from large, regional smoke plumes may limit the potential for pyroCb development when these plumes pass over blow-up fires downwind. Future work is required to determine how these variables contribute to plume structure and behavior that ultimately initiates or suppresses pyroCb development^{24,25} and injection of smoke particles into the stratosphere.

Initial stratospheric smoke plumes

Lower-stratospheric smoke plumes injected by both phases of ANYSO were transported to the east of Australia (Fig. 2a, b), within the eastward progressing high pressure ridge. Satellite observations of these nascent plumes represent distinct, individual stratospheric injections and source terms. The corresponding

quantitative information (summarized in Supplementary Tables 2 and 3) facilitates a direct comparison with the PNE smoke plume (Fig. 2c). These observations also set a foundation for future modeling studies to understand potential downstream impacts on atmospheric chemistry, radiation, and dynamic circulation.

The Cloud-Aerosol Lidar with Orthogonal Polarization (CALIOP), flown aboard NASA's polar-orbiting CALIPSO satellite⁵⁷, passed over the young stratospheric smoke plume from ANYSO's first phase several times, revealing a mixture of ice and smoke particles above the tropopause (Supplementary Fig. 7). By 02 January (01:40 UTC, 43 h after pyroCb cessation), ice crystal presence within the plume had diminished, revealing a distinct residual smoke layer averaging 3.5 km deep in the lower stratosphere (Fig. 7). This observation occurred ~17 h before plume transport was influenced by the dynamics of a large mid-latitude cyclone (Fig. 2a). A similar CALIOP profile for ANYSO's phase-two plume shows a residual smoke layer averaging ~3.5 km in depth ~72 h after pyroCb cessation (Fig. 8). Smoke particle mass densities in the stratosphere were estimated at 40–140 $\mu\text{g m}^{-3}$ for phase one and 13–47 $\mu\text{g m}^{-3}$ for phase two² (see Methods section).

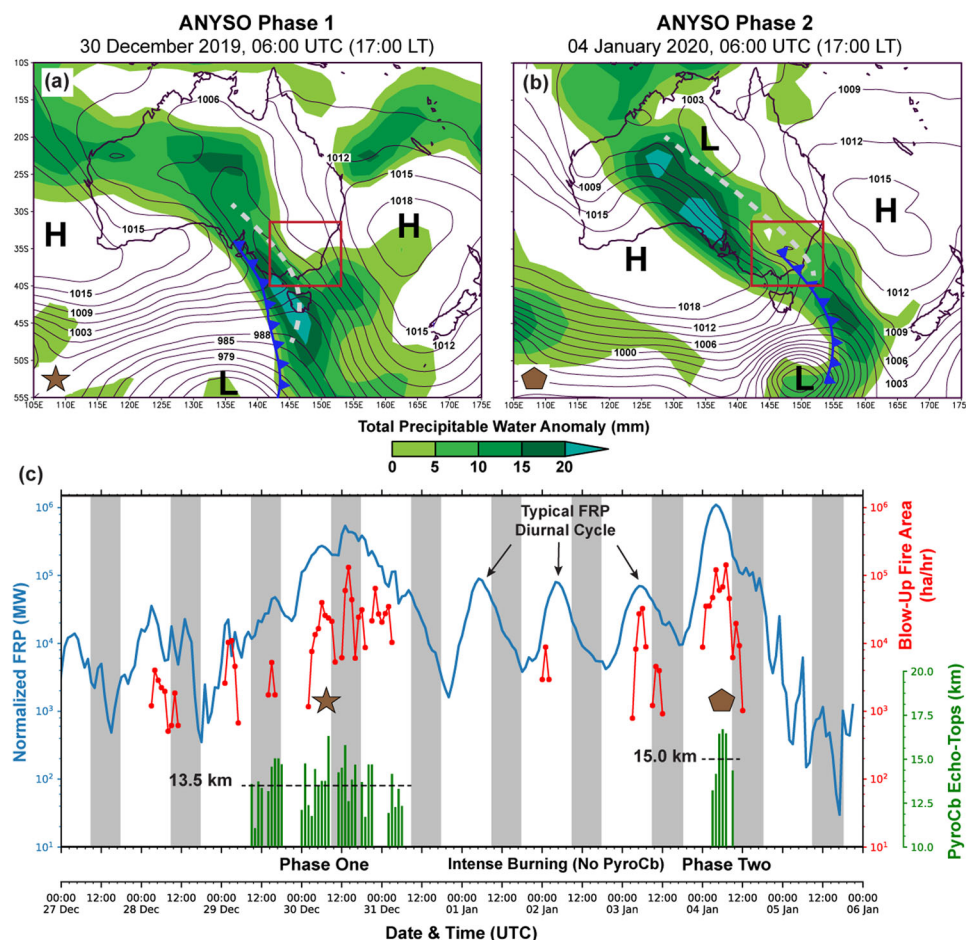


Fig. 6 Meteorology driving ANYSO pyroCb activity, regional fire activity, and timing. Maps in **a** and **b** display the primary synoptic weather features as both phases of pyroCb activity reached maximum intensity, with cold fronts displayed in blue and prefrontal troughs in dashed gray. Green shading indicates positive anomalies of total column precipitable water derived from the 30-year (1981–2010) NCEP/NCAR climatology. Mean sea level pressure is displayed in black contours. Red box indicates the region with active wildfires and pyroCb development analyzed in the hourly time series (**c**). Normalized FRP from AHI is plotted in blue. The area burned per hour by active blow-up fires is plotted in red. Maximum pyroCb echo-tops are plotted in green, with the approximate tropopause altitude represented as a dashed black line. Symbols coincide with the timing of the synoptic weather maps in **a** and **b**.

Following previous studies^{2,29}, the horizontal extent of both stratospheric plumes was estimated using observations of Ultra-Violet Aerosol Index (UVAI, dimensionless) retrieved from the Ozone Mapping Profiler Suite (OMPS) Nadir Mapper, flown aboard the Suomi National Polar-orbiting Partnership (S-NPP) satellite⁵⁸. UVAI is sensitive to the altitude of light-absorbing smoke particles in the stratosphere (e.g., black and brown carbon), corresponding with the largest values (e.g., >15–20)^{22,29}. Comparison with CALIOP profiling for both ANYSO plumes (Figs. 7 and 8) showed that pixels with a UVAI at or above 15 were consistent with smoke particles in the stratosphere, which mirrors the UVAI thresholds applied to the 2001 Chisholm and 2017 PNE smoke plumes^{2,29}. Integration of each individual pixel area with a UVAI exceeding 15 yielded an instantaneous stratospheric smoke plume area of 1.6 million km² for phase one and 1.1 million km² for phase two.

The PNE plume coincided with the largest UVAI values observed to date for any stratospheric aerosol plume worldwide² (40–50+), which is significantly larger than the UVAI observed early in the lifetimes of both ANYSO plumes (25–44, Supplementary Figs. 8 and 9). The PNE plume also coincided with larger mass density values (73–220 $\mu\text{g m}^{-3}$). However, when compared with the PNE, the ANYSO phase one plume occupied a much larger volume in the stratosphere at about the same time period after pyroCb cessation (48 h). Estimated smoke particle mass (0.2–0.8 Tg) was

therefore about twice as large as the PNE (0.1–0.3 Tg), despite coinciding with a lower mass density (Fig. 3).

Downwind plume evolution and persistence

Over the weeks and months following ANYSO, the ensuing stratospheric plumes encircled the Southern Hemisphere between 20°S and 90°S. The OMPS Limb Profiler (LP) instrument tracked the downwind evolution of the stratospheric aerosol vertical profile and its persistence. OMPS LP aerosol extinction coefficient (at 997 nm, see Methods section) averaged between 20°S and 90°S increased by a factor of five between 15 and 20 km during the first few months after ANYSO (~ 0.0005 – 0.0015 km^{-1} ; Fig. 9a) compared with pre-injection background values (0.0001 – 0.0003 km^{-1}). The estimated e-folding aerosol decay time for the ANYSO plume at altitudes below 18 km (120–150 days) was similar to that of the PNE plume⁸. However, it nearly doubled to 250–350 days at altitudes above 19 km (Supplementary Fig. 10). Stratospheric aerosol extinction above this altitude persisted at values 150% higher than background (December 2019) for at least 15 months after initial injection (through March 2021; Fig. 9a), far exceeding the stratospheric lifetime of the PNE smoke plume^{8,59}. ANYSO therefore set a new benchmark for detectable smoke plume residence time in the stratosphere.

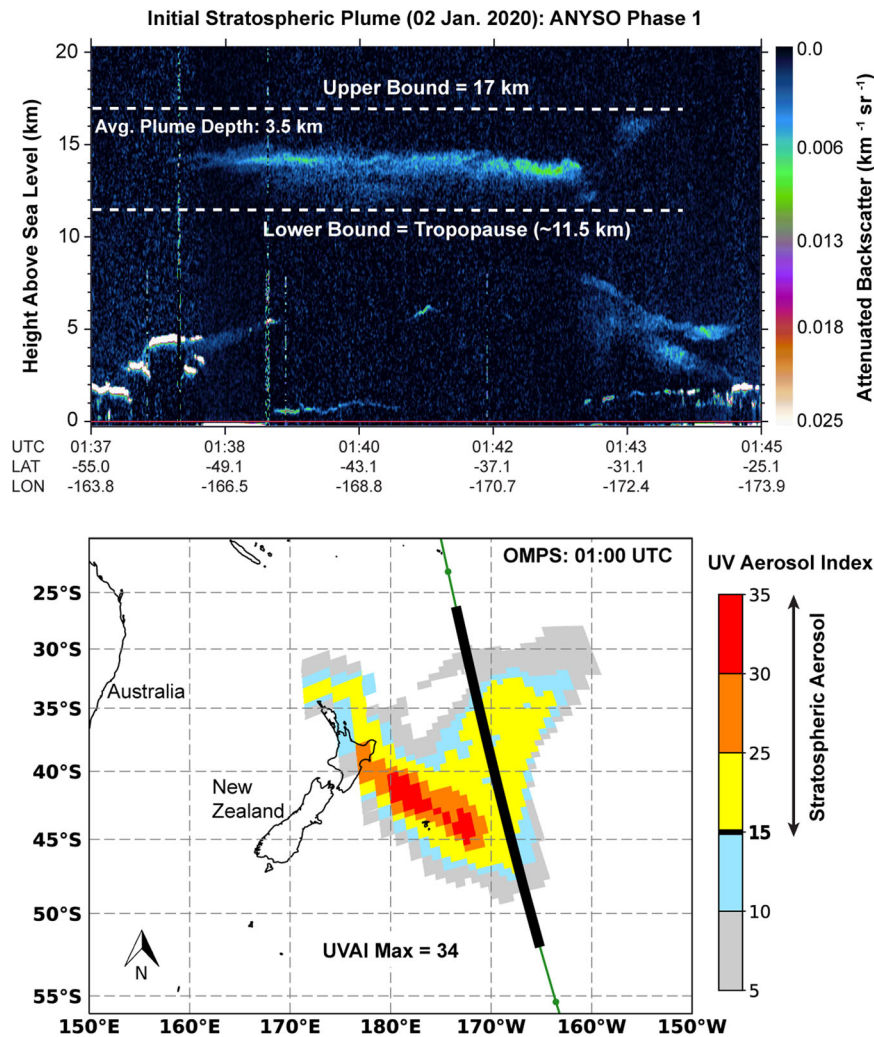


Fig. 7 Characteristics of the initial phase one stratospheric smoke plume. Top panel shows profiles of 532 nm attenuated backscatter ($\text{km}^{-1} \text{sr}^{-1}$) observed by CALIOP on 02 January 2020 for a daytime (ascending) CALIPSO overpass beginning 01:37 UTC. Dashed white lines denote the approximate upper and lower bounds of the plume. Bottom panel shows near-coincident ultra-violet aerosol index (UVAI) observations from OMPS. The CALIPSO satellite track is superimposed green, with black indicating the segment used in the top panel. The horizontal extent of the stratospheric smoke plume ($\text{AI} \geq 15$) is displayed in shades of yellow and red.

Smoke particles (e.g., black carbon) in a pyroCb smoke plume absorb solar radiation, warming the layer of the stratosphere where they reside. The resulting diabatic heating effect generates instability, causing the plume to rise after its initial injection into the stratosphere⁸. The ‘diabatic lofting’ effect is often strong enough to oppose the mean downward motion of the UTLS Brewer–Dobson circulation⁶⁰ over the mid- and high latitudes, ultimately increasing plume lifetime in the stratosphere. OMPS LP reveals that the altitude of the ANYSO plume increased from its initial injection at 14–17 km to 34 km within 40 days (Fig. 9a), extending well into the ozone layer. These extreme altitudes are the highest ever reached by a wildfire smoke plume in the historical record to date. As described by previous studies¹, the ANYSO plume even rivals the altitudes reached by the sulfate plumes ensuing from climate altering volcanic eruptions, such as Mt. Pinatubo in 1991, which reached 30–40 km^{35,36}. For comparison, the 2017 PNE plume (previous benchmark) ascended from 12–14 km to ~23 km⁶.

Figure 9b depicts zonally averaged aerosol extinction profiles on 26 March 2020, highlighting a very complicated aerosol particle distribution in the global stratosphere. The ANYSO smoke is easily distinguished by the magnitude of aerosol extinction in the stratosphere south of ~30°S, and by the diabatic lofting of smoke

particles above 25 km in several latitude bands. These high-altitude smoke observations likely coincide with at least three persistent, blob-like smoke features that not only continued rising over time (~34 km, potential temperature of 950 K), but also directly altered wind patterns in the stratosphere^{1,30,31}. Temperature perturbations in the layers affected by absorbing smoke particles generated potential vorticity (positive anomaly), which ultimately induced anticyclonic circulation anomalies in the stratosphere for several weeks^{30,31}. Enhanced anticyclonic rotation was also observed with the PNE plume in the Northern Hemisphere stratosphere, evidenced by destruction of positive potential vorticity (negative anomaly)³¹. This new discovery motivates the reexamination of previous pyroCb smoke plumes to determine how often they influence dynamic circulation in the stratosphere. More importantly, it highlights the consequence of increasingly greater stratospheric smoke injections from pyroCb outbreaks, and potential for even greater perturbations to hemispheric circulation should their scale and intensity increase in the future.

Comparison and potential interaction with volcanic plumes

An analysis of stratospheric aerosol optical depth (sAOD, 869 nm) retrieved from OMPS LP across all available latitude bands (Fig. 10)

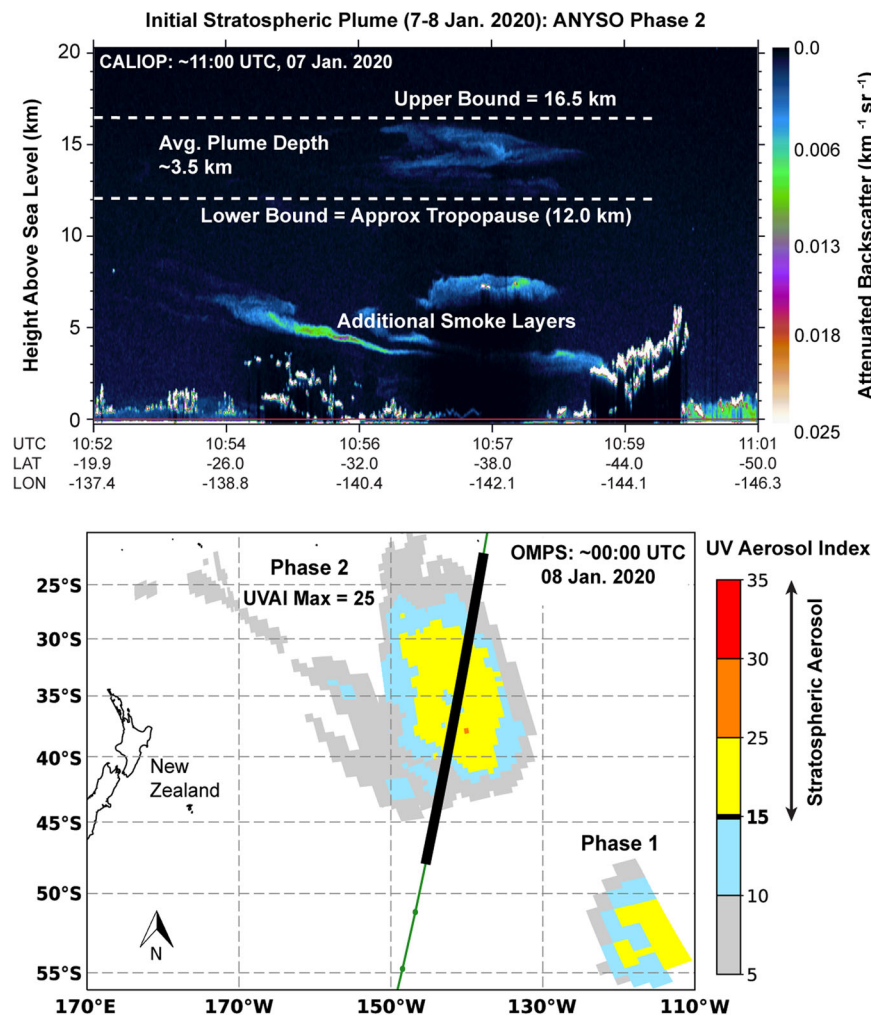


Fig. 8 Characteristics of the initial phase two stratospheric smoke plume. Top panel shows profiles of 532 nm attenuated backscatter ($\text{km}^{-1} \text{sr}^{-1}$) observed by CALIOP on 07 January 2020 for a nighttime (descending) CALIPSO overpass beginning 10:52 UTC. Dashed white lines denote the approximate upper and lower bounds of the plume. Bottom panel shows ultra-violet aerosol index (UVAI) observations from OMPS on 08 January 2020 at 00:00 UTC, which is ~13 h after the CALIOP observations in the top panel. The corresponding CALIPSO satellite track is superimposed green, with black indicating the segment used above. The horizontal extent of the stratospheric smoke plume ($\text{AI} \geq 15$) is displayed in shades of yellow and red.

reveals that the majority of significant stratospheric aerosol plumes in recent years originated from volcanic eruptions (Nabro 2011, Kelut 2014, Calbuco 2015, Aoba 2018, Ulawun 2019, and Raikoke 2019)⁶¹. However, the large pyroCb smoke plumes from the ANYSO and PNE are also clearly distinguished. The impact from ANYSO is particularly large, with sAOD reaching 0.015. Since 2012, this was only exceeded by the 2019 Raikoke eruption, which affected the Northern Hemisphere stratosphere (Fig. 9b) and produced sAOD values of 0.025 (Fig. 10). The lifetime of the ANYSO plume is at least 15 months through the end of March 2021, which is comparable with Raikoke and the 2015 Calbuco eruptions⁶². For comparison, the 2017 PNE produced a maximum sAOD of 0.008 and dissipated after ten months⁵⁹. The sAOD values for both pyroCb events (ANYSO and PNE) easily exceeded those of the Kelut (2014), Aoba (2018), and Ulawun (2019) eruptions. Two of the four largest stratospheric plumes observed since 2012 therefore originated from regional outbreaks of intense pyroCb activity. Figure 10 also reveals shorter periods of elevated sAOD north of 45°N during the Northern Hemisphere fire seasons of 2014, 2015, 2018, 2019, and 2020, which may be a result of ‘typical’ seasonal pyroCb activity^{2,20–23,56}.

While large and intense pyroCb outbreaks are a relatively new phenomenon, they account for almost one third of the sAOD

budget during 2017–2020. The highest levels of sAOD observed during the entire 25 year, post-Pinatubo era were observed during 2019–2020⁶¹, with ANYSO playing a significant role in reaching that milestone (Fig. 10). However, several volcanic eruptions also contributed. Figures 9b and 10 indicate that stratospheric smoke from ANYSO likely mixed with the residual volcanic plume from the earlier Ulawun eruption in Papua New Guinea (26 June 2019)⁶³. While this is especially evident in the tropics, the mid- and high latitudes of the Southern Hemisphere also contained diffuse remnants of the Ulawun plume prior to ANYSO. Poleward transport of this volcanic plume (and others) is evidenced in Supplementary Fig. 11, which provides a corresponding display of aerosol extinction at three stratospheric altitudes. Similarly, portions of North America and Siberia experienced prolific pyroCb activity during 2019 and 2020, which likely contributed to the elevated sAOD values following the Raikoke eruption. The potential for increasing pyroCb activity during the summer fire seasons in each hemisphere (approximately six months apart) therefore has significant implications for future stratospheric aerosol behavior, including potential interactions with sulfate-based plumes originating from volcanic eruptions. Detailed examination of

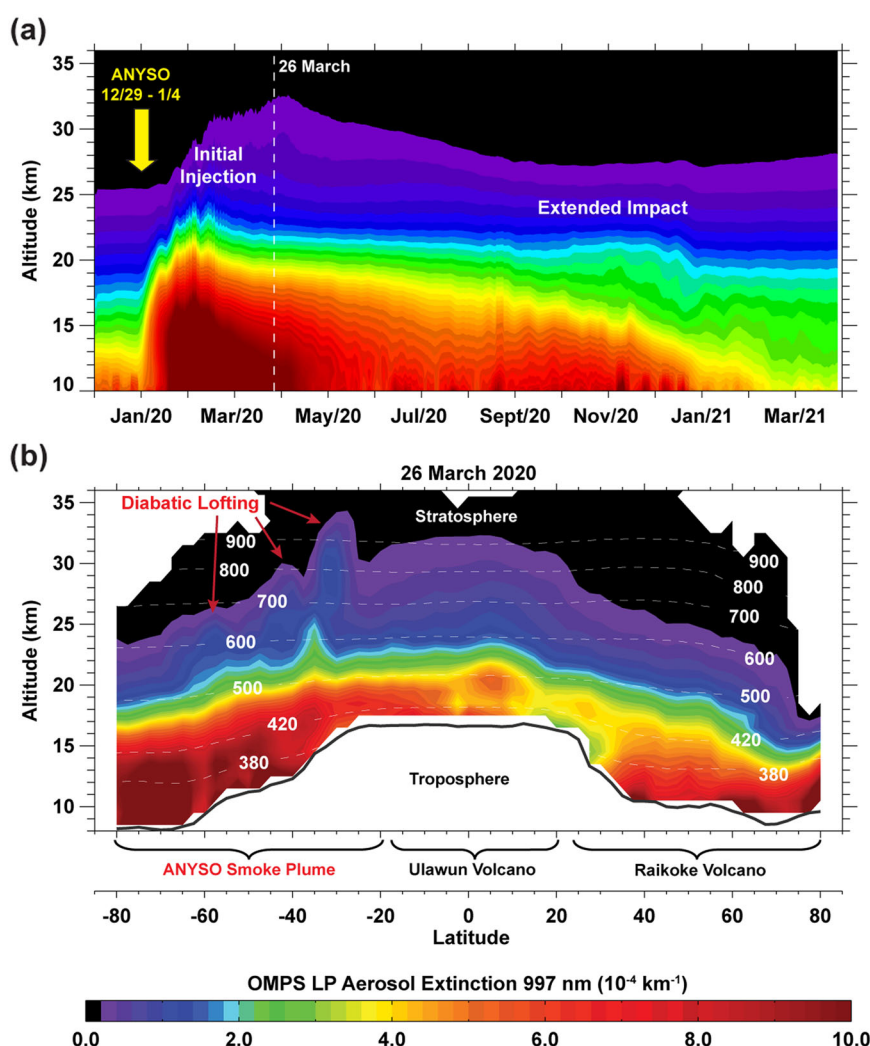


Fig. 9 Smoke plume evolution and persistence in the stratosphere. **a** Daily aerosol extinction profiles at 997 nm between 20°S and 90°S measured by OMPS LP from 01 December 2019 through 29 March 2021. The display is only for profiles in the stratosphere, measured at least 1 km above the mean tropopause altitude. **b** Zonally averaged aerosol extinction profiles at 997 nm, calculated for 2.5° latitude bands on 26 March 2020. The black line denotes the mean tropopause altitude and the white contours are mean potential temperature (K). The primary source of stratospheric aerosols in certain latitude bands is specified at the bottom.

this complex stratospheric aerosol loading situation will be explored in future studies.

DISCUSSION

This study provides a quantitative analysis of the intense fire and pyroCb activity observed during the Australian New Year Super Outbreak (ANYSO) in southeastern Australia, revealing that 13 blow-up fires contributed to 38 distinct, ice-capped convective columns, defined as pyroCb pulses. Two distinct phases of ANYSO pyroCb activity resulted in two of the three largest smoke particle injections into the lower stratosphere observed through March 2021, rivaling or exceeding the stratospheric impact from all volcanic eruptions observed during 2012–2020. The large stratospheric smoke plumes ensuing from ANYSO reached altitudes higher than smoke has ever been observed, encircled a portion of the Southern Hemisphere, altered dynamic circulation^{1,30,31} and persisted for more than 15 months. Fewer than 3 years earlier, the Pacific Northwest Event (PNE) in Canada produced a persistent smoke plume that encircled a portion of the Northern Hemisphere². These regional pyroCb outbreaks represent a new class of

stratospheric smoke plumes with the potential for significant climate feedbacks on seasonal and hemispheric scales. Large pyroCb outbreaks also serve as validation for nuclear winter theory, which is based on smoke from burning cities rising into the stratosphere and encircling the globe^{8,37,64}. The extreme scale of ANYSO therefore motivates a variety of future modeling work to understand the impact of stratospheric smoke plumes on surface cooling, stratospheric chemistry, and dynamic circulation.

Many regions worldwide have experienced extremely active fire seasons and prolific pyroCb activity over the past four years (2017–2020), including Canada, Alaska, eastern Siberia, and the western United States. PyroCb outbreaks likely represent a growing severe weather hazard in many of these fire prone regions, presenting hazards for commercial aviation¹⁷ and all forms of firefighting, including both ground and airborne support^{38,65,66}. ANYSO was driven by weather conditions similar to several previous extreme events^{2,21,23–25}, suggesting that intense pyroCb activity, ensuing stratospheric smoke plumes, and related hazards are predictable in a changing climate.

The exceptional duration of ANYSO's first phase (10 blow-up fires producing 33 pyroCb pulses over ~45 h) resulted in part

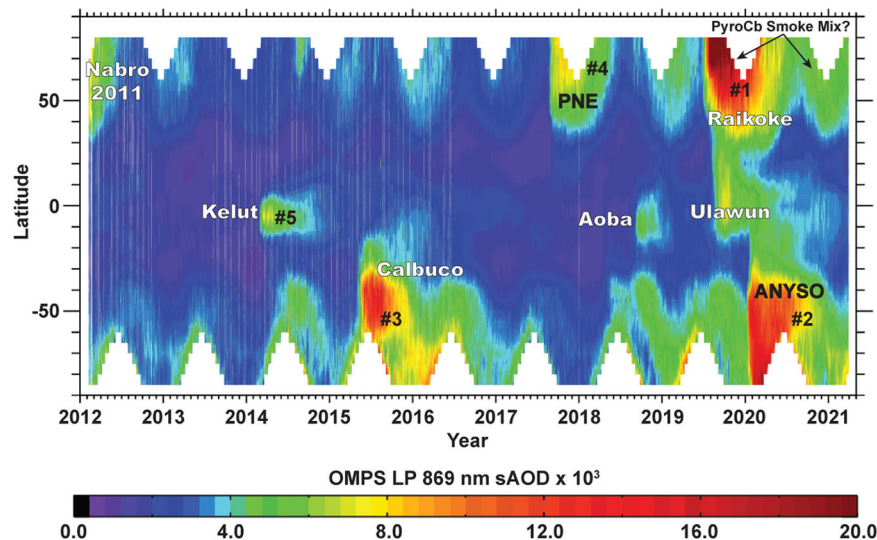


Fig. 10 Comparing ANYSO with all significant stratospheric plumes observed during 2012–2021. Shading indicates daily OMPS LP stratospheric aerosol optical depth (sAOD) calculated in five degree latitude bands using extinction profiles at 869 nm. White labels indicate volcanic plumes and black labels indicate pyroCb smoke plumes. Numbers rank the five largest plumes in this record based on maximum sAOD.

from slow progression of large-scale weather features that set the stage for thunderstorm development over active fires. A combination of intense wildfire activity and conducive meteorology was also a key factor driving pyroCb development during the PNE². This motivates future studies to identify regions with a high frequency of meteorological conditions supportive of these unusual thunderstorms, especially concurrence with the most active parts of the local fire season. Improved understanding of these mechanisms will facilitate advanced warning of future pyroCb outbreaks and ensuing stratospheric smoke plumes.

As environmental conditions become more supportive of severe fire seasons^{9,10}, it is logical to expect a higher frequency and larger magnitude of pyroCb outbreaks, reflecting increased coupling of the mixed layer with surface conditions (e.g., more blow-up fires). However, the concurrence of this fire activity with meteorology favorable for thunderstorm development is likely to be a limiting factor in some regions. The recurrence interval of pyroCb outbreaks also reflects the characteristics and availability of fuels. In southeastern Australia, previous studies show that the mitigating effect of prior fire activity on extreme wildfire occurrence is limited⁶⁷. Therefore, while the fires observed during the Black Summer of 2019/20 burned at least 20% of the forests in the ANYSO region⁶⁸, sufficient fuels will likely be in place during the next period of conditions favorable for a pyroCb super outbreak.

The exceptional magnitude of ANYSO has initiated a new phase of pyroCb research aimed at understanding larger scales of potential atmospheric impacts and climate feedbacks. ANYSO also revealed that a pyroCb super outbreak can significantly augment the global stratospheric aerosol loading induced by preceding volcanic eruptions, raising new questions on future aerosol behavior in the stratosphere. Recent field experiments provide a wealth of new in situ and remotely sensed observations of individual pyroCb pulses and high-altitude smoke plumes^{16,17,69} to facilitate improved climate modeling studies (<https://earthobservatory.nasa.gov/images/145446/flying-through-a-fire-cloud>). With these observations and the new insights from ANYSO, there are sure to be new discoveries as research continues to explore the role of pyroCb activity in the climate system.

METHODS

Stratospheric smoke particle mass from lidar (top-down estimate)

The primary method applied to estimate smoke particle mass injected into the stratosphere by pyroCb activity requires the combination of ‘top-down’ CALIOP vertical profiling and UVAI observations, which were obtained from the OMPS Nadir Mapper (NM). These calculations were based on observations two to four days after pyroCb cessation (Supplementary Table 2), when the stratospheric plume was comprised primarily of residual smoke aerosol rather than ice particles. Regional tropopause heights were determined using temperature profiles from local radiosondes. Accompanying dynamic tropopause maps reveal minimal variation in tropopause altitude to east of Australia, where the nascent smoke plumes were transported (Supplementary Figs. 3 and 5). The vertical extent of the plume above the tropopause was constrained using vertical profiles of 532 nm backscatter and linear laser depolarization ratio from CALIOP. The average particle mass density (M_p) of the stratospheric smoke layer was calculated by:

$$M_p = \frac{\beta R}{\epsilon} \quad (1)$$

where β is the average CALIOP Level 1 backscatter (units of $\text{m}^{-1} \text{sr}^{-1}$) of all pixels coinciding with stratospheric smoke, R is an assumed particulate extinction-to-backscatter lidar ratio (units of sr), and ϵ is the particle mass extinction coefficient (units of $\text{m}^2 \text{g}^{-1}$). To account for a potential mix of smoke particles, water/ice, and mineral dust, a range of 3.0 to $6.0 \text{ m}^2 \text{g}^{-1}$ was used for ϵ and a range of 40 to 70 sr was used for R ^{5,70}. Output is therefore provided in an uncertainly range, based on the sensitivity of M_p to the values of ϵ and R , which are dependent on the physical and optical properties of smoke particles².

The horizontal area of ANYSO's initial plumes was constrained using UVAI from OMPS NM. By pairing these data with CALIOP profiles, a UVAI threshold of 15 was diagnosed to identify pixels containing stratospheric smoke. The total area of OMPS NM pixels above that threshold was used as an estimate of the horizontal extent of the stratospheric plume^{2,29}. Integration of M_p over the smoke plume area and depth (diagnosed from CALIOP profiles and assumed constant over the horizontal extent of the plume) provided an estimate of the total smoke particles mass injected into the stratosphere by each phase of ANYSO.

The upper bound of 70 sr for R provides consistency with several existing studies on pyroCb smoke plumes, including ANYSO³⁰. This is slightly higher than the upper bound applied in our previous study of the PNE plume (60 sr)². However, ground-based lidar observations of the ANYSO plume as it passed over South America reveal significantly larger R values at 532 nm ranging from 75 sr to 112 sr⁷¹. The cumulative particle

mass estimate provided in Fig. 3 (0.3–1.1 Tg) increases to 0.5–1.6 Tg when applying these larger values.

The CALIPSO orbit missed the core of the stratospheric plume on 02 January (Fig. 7), suggesting that the mass estimate for ANYSO phase one may be slightly underestimated (due to a weaker β), regardless of the range applied for R . Similarly, the lack of near-coincident CALIOP and OMPS NM observations of the ANYSO phase two plume introduces additional uncertainty into the corresponding mass estimate. When considering that CALIOP (nighttime) preceded OMPS NM (daytime) by ~13 hr on 7–8 January (Fig. 8), β likely represents observations near the edge of the plume. These phase two observations (70–90 hr after pyroCb cessation) are also at least a day later than the observations of ANYSO phase one and the PNE (~48 hr after pyroCb cessation). When considering that UVAI values generally decrease with time, application of the same UVAI threshold of 15 to ANYSO phase two may underestimate plume area and the resulting particle mass. Sensitivity of pyroCb smoke particle mass estimates to UVAI thresholds and observation timing will be explored in a future study. The comparison with 'typical pyroCb activity' in Fig. 3 is simply a combined range of similar mass estimates from pyroCb plumes analyzed during the 2013 fire season in Western North America (coniferous forest)^{2,20}.

Stratospheric smoke particle mass from UVAI (top-down estimate)

The second top-down mass estimate method applied here is based entirely on UVAI observations (again from OMPS NM, Supplementary Table 3), which facilitates analysis of stratospheric particle mass within the first 24 hr after pyroCb cessation or even while the event is still ongoing (e.g., ANYSO's first phase). It employs a linear relationship between UVAI and extinction aerosol optical depth (extAOD) previously identified for the Chisholm smoke plume²⁹, allowing the mass of stratospheric aerosol particles per-pixel (M_p) to be calculated by

$$M_p = \frac{\text{extAOD} \times A_p}{\epsilon} \quad (2)$$

where A_p is the OMPS NM pixel area and ϵ is the particle mass extinction coefficient. Following the lidar-based method described above², a range of 3.0–6.0 m² g⁻¹ was used for ϵ . The stratospheric horizontal area of both initial pyroCb plumes was also constrained using the same UVAI threshold of 15 (refs. ^{2,29}). Integration over the full smoke plume area provided an estimate of the total smoke particle mass injected into the stratosphere.

The early, post-injection period targeted by this method often involves a complicated mix of freshly injected smoke particles and cloud ice (i.e., decaying pyroCb anvil clouds), which likely introduces some uncertainty into the resulting particle mass estimates. For example, the first OMPS NM UVAI observation of the phase one plume occurred ~3 h before pyroCb cessation on 31 December (Supplementary Fig. 8), revealing that at least 0.1–0.3 Tg of smoke particle mass was already in the stratosphere. However, this early observation included several pyroCb anvil clouds that were still intact or developing, and therefore does not serve as a direct comparison with the lidar based approach in Fig. 7. The phase one plume was split across multiple OMPS NM orbits on 01 January, which prevented a second rapid mass estimate using this method.

The first UVAI observations of the phase two plume occurred ~17 h after pyroCb cessation (Supplementary Fig. 9), yielding 0.1–0.3 Tg of particle mass in the stratosphere. This UVAI-based estimate overlaps with the range provided by the lidar-based approach (0.1–0.2 Tg, Fig. 3). When considering the potential for underestimated smoke mass as described above, the UVAI method upper bound of 0.3 Tg was used in this study (Fig. 3). The UVAI method was also applied to estimate the smoke particle mass injected by previous significant events in Australia, including Black Saturday⁷² and the Great Divide event⁷³ (Fig. 3).

Fire burned area estimates

Fire burned area estimates for the ANYSO blow-up fires (Fig. 1), were estimated from a variety of remotely sensed data sources. Active fire detections served as a base layer via the MODerate Resolution Imaging Spectroradiometer (MODIS) instrument aboard the Terra and Aqua satellites⁷⁴. Pixels with elevated FRP (above 127 MW) were used as markers for the elevated heat output from blow-up fires. Pseudo-elliptical areas, with typically elevated Normalized-Difference Burn Index (NDBI) imagery (NSW Government and Victorian Government)⁷⁵, either in absolute terms or relative to surrounding burnt areas, were used to refine blow-up area extents. Deep flaming was occasionally confirmed from Sentinel 2 imagery

(<https://www.sentinel-hub.com/>). Bureau of Meteorology (BoM) weather radar data (mainly from Wollongong, Canberra, and Bairnsdale) were used as an additional confirmation of blow-up activity, when a convective core (identified from reflectivity level) was stationary over a given fire. For more information on BoM weather radar, please see the methods section on echo-top data.

Blow-up fires were assumed to occur exclusively in regions dominated by forest vegetation, as fires in Australian grassland fuels do not produce sufficiently intense or persistent pyro-convection. However, blow-up fires in forest fuels may still leave insufficient fire ground residual heat to satisfy the MODIS fire detection algorithm in subsequent overpasses. The boundaries of large fire detection gaps within a blow-up area (typically covering over 20 km²) were therefore constrained with NDBI mapping. This combined approach set the foundation for estimating the area burned by all blow-up fires observed during ANYSO, which often served as a pyroCb source. Weather radar and Sentinel 2 imagery were used when available or applicable as additional constraints.

Production of a consistent database for fire areas, including blow-up fires, across multiple jurisdictions is a long-term goal in Australia. Research efforts are still underway. The estimated fire expansion in Fig. 6c employed this ongoing research for the set of ANYSO blow-up fires by assigning 60% of the burnt area to the hour of peak estimated intensity from the data sources discussed above, with 20% assigned to the hour on either side. These values were then accumulated over the southeastern Australia study region for each hour. While superior data sources may exist for individual fires (e.g., airborne mapping), they are not consistently available across all fires in all jurisdictions within southeastern Australia.

A variety of factors may affect this approach, including MODIS pixel resolution, MODIS return-intervals, cloud cover, dense smoke in imagery, parallax error, and radar coverage. However, the impact from these combined factors was considered acceptable in the basic, regional-scale estimates applied in this study. It is also acknowledged that active fire containment efforts by Incident Management Teams (e.g., burn-outs, back-burns, aerial suppression) may confound later interpretation of remotely sensed data, which is based on a priori expectations of fire spread.

Mass of biomass consumed and energy released (bottom-up estimate)

The total area burned in the Australia fire season exceeded 7 million ha (ref. ⁴), but bottom-up smoke mass estimates were only based on the fraction from the specific dates with pyroCb activity and the 530,000 ha burnt by the 13 blow-up fires identified as pyroCb sources (methods described above). The total fuel loading in Australian forested areas is on the order of 300,000 kg of dry biomass per ha (ref. ⁴), which includes tree trunks and soil carbon that are only partially consumed by even severe wildfires. By assuming a range of potential fuel consumption of 15,000 to 60,000 kg ha⁻¹, equivalent to 5–20% of total biomass (measurements of near-surface non-trunk fuels fall near the bottom of this range, averaging ~20,000 kg ha⁻¹)⁷⁶, these 13 blow-up fires are estimated to have consumed a total 7.9–38.8 Tg of fuels. These values were converted to mass of particulate matter with a diameter of <2.5 μ m (PM_{2.5}) using emission factors of 16.9–38.8 grams PM_{2.5} per kilogram dry fuel consumed⁷⁷ based on measurements of smoke from open burning in eucalyptus. The resulting ground-based estimate of PM_{2.5} release from the blow-up fires ranges from 0.1 to 1.2 Tg. Similar to previous studies², this bottom-up estimate appears low relative to the top-down estimate (0.3–1.1 Tg, top-down methods described above). While recent modeling work does suggest that emission factors of PM_{2.5} may be much greater than climatological averages during extreme fire events⁷⁸, future study is required to examine direct correspondence between blow-up fires, greater fire severity, and more fuels consumed.

To estimate the energy released by the 13 blow-up fires driving pyroCb development, we assumed an effective heat of combustion of 18,700 kJ kg⁻¹, which is similar to previous studies¹¹, and laboratory data from eucalyptus fuels⁷⁹. Multiplying by the total mass of fuel consumed (7.9–38.8 Tg) yields an estimated energy release of 1.3–5.1 $\times 10^{14}$ kJ. This estimate represents a maximum value for sensible energy release. It does not account for the substantial fraction of combustion that is expended to heat adjacent fuels and boil off fuel moisture, some of which is available as latent heat, and converted to sensible heat higher in the atmospheric column. The TNT and atomic bomb equivalents were based the heat of combustion of TNT of 4 kJ g⁻¹, with one Hiroshima atomic bomb estimated at ~15 kT of TNT.

OMPS LP data processing

OMPS LP retrieves aerosol extinction profiles at 510, 600, 674, 745, 869, and 997 nm wavelengths⁸⁰. In addition, it provides some information about cloud height and type, which is used to identify enhanced aerosol layers in the stratosphere. The OMPS LP sensor uses three vertical slits separated horizontally by 250 km, to provide near global coverage and more than 7000 profiles a day. All OMPS LP analysis is based on data from the center slit, which has the most accurate calibration and straylight correction⁸⁰. The temperature, pressure, and tropopause altitudes are derived from the geopotential height product provided by the NASA Global Modeling and Assimilation Office operational model, and these fields are included in OMPS LP Level 2 daily files.

OMPS LP aerosol extinction profiles at 997 nm were aggregated at 1-day intervals for all measurements above the tropopause between 20°S and 90°S, and smoothed spatially using five points boxcar averaging to remove any outliers (Fig. 9a). With this methodology, aerosol extinction values at lower altitudes (e.g., 10 km) primarily represent observations at high latitudes. Estimated *e*-folding aerosol decay times were calculated using an exponential fit of OMPS LP aerosol extinction measurements at a range of altitudes above the tropopause, with the background aerosols removed. The background aerosol extinction profile was defined as the mean aerosol extinction during December 2019, prior to ANYSO.

Zonally averaged aerosol extinction profiles at 997 nm (Fig. 9b) were calculated for 2.5° latitude bands on 26 March 2020. When considering OMPS LP observing geometry, 997 nm is considered to be the most sensitive wavelength to aerosols in the Southern Hemisphere and lower altitudes, where the Rayleigh scattering is high⁸⁰. However, measurements at 997 nm are only available after 26 November 2013. The stratospheric aerosol optical depth (sAOD) daily time series were derived by integrating aerosol extinction profiles above the tropopause and averaging every five degrees of latitude (Fig. 10). Aerosol extinction profiles at 869 nm were used to create the sAOD time series because measurements at that wavelength are available throughout the OMPS LP data record.

PyroCb detection from satellite

The duration of ANYSO was analyzed at 10 min intervals using AHI (e.g., Fig. 5). A key defining characteristic of pyroCb activity is the presence of large anvil ice clouds in the UTLS. PyroCb detection therefore requires cloud top BT₁₁ to be lower than an approximated homogeneous liquid-water freezing threshold of −35 °C (ice cloud). During nighttime, pyroCb activity was identified exclusively using BT₁₁, with intense updrafts coinciding with the lowest (i.e., coldest) values below the −35 °C pyroCb threshold. During daytime, a previously developed algorithm²⁰ was applied to take advantage of unusually small particles existing at the tops of pyroCbs, which result from a large quantity of available cloud condensation nuclei in the form of smoke particles (indirect aerosol effects)¹³. Differences in brightness temperatures at 3.9 μm and 11.0 μm become unusually large (near and greater than 50 K) in the presence of such smaller particles. The algorithm is therefore able to effectively distinguish pyroCb activity from traditional thunderstorms in the vicinity of active fires. Imagery products based on these methods are posted in near-real-time on the Naval Research Laboratory's pyroCb website: <http://www.nrlmry.navy.mil/pyrocb-bin/pyrocb.cgi>.

Radar echo-tops

Australia BoM level 2 weather radar were used for echo-top analysis. Two sites were employed, Bairnsdale (Victoria, 37.89° S, 147.56° E) and Captain's Flat (New South Wales, 35.66° S, 149.51° E). Temporal resolution between full volume scans is 6 and 10 min for Captain's Flat and Bairnsdale, respectively. Captain's Flat data were degraded to the Bairnsdale time grid. These data were retrieved from the National Computational Infrastructure portal maintained by Australian National University (<http://dapds00.nci.org.au/thredds/fileServer/rq0>). Echo-tops were determined from each scan volume at all columns between 5 and 200 km from the radar site. For each column, the echo-top was identified as the height of the top-most vertical mid-point of three consecutively stacked range bins with reflectivity >10 dBZ, subject to the condition that this height was >8 km in altitude. While the majority of the radar echo-top signal is assumed to result from hydrometeors (primarily ice), it is possible that large pyrometeors (ash and other large debris) were also mixed in⁸¹. Weather radar is generally not sensitive to small smoke particles (PM_{2.5}) in the high-altitude pyroCb outflow (i.e., anvil cloud).

PyroCb echo-top assignment was determined by a search box of 0.20° latitude and 0.25° longitude centered on the location of pyroCb anvils identified by the AHI BT₁₁ data described above. All 18 ANYSO pyroCb sub-events were within range of either Bairnsdale or Captain's Flat. PyroCb echo-tops from all phase one sub-events were obtained from Bairnsdale, except #10, 13, and 14 from Captain's Flat. Echo-tops for all phase two sub-events were obtained from Captain's Flat, except #16 from Bairnsdale. Echo-top potential temperature was calculated by linear interpolation using the radiosonde profile (temperature, height, and potential temperature) closest in time to each radar observation. These data were primarily retrieved from the Melbourne radiosonde site, available at <http://weather.uwyo.edu/upperair/sounding.html>. The Wagga Wagga radiosonde site is closer to the ANYSO region, but its data archive is not as comprehensive. Thermodynamic profiles from Wagga Wagga therefore served as a supplement to those obtained from Melbourne.

Fire radiative power

FRP data referenced in this study are based on observations from AHI at 10 min intervals (Fig. 5). FRP was obtained from the Wildfire Automated Biomass Burning Algorithm (WFABBA) as applied to AHI data. The WFABBA uses the difference in ~4 μm (AHI Channel 7) radiance space between the fire pixel and the estimated background to derive FRP, following the techniques used with Advanced Baseline Imager (ABI) on the current generation of GOES satellites^{82–85}. The similarities between ABI and AHI allow for straightforward application of the WFABBA to AHI fire detection and characterization. The WFABBA provides FRP for the majority of detected fire pixels. However, cloud cover can occasionally prevent WFABBA retrieval of FRP data^{84,85}.

The hourly FRP time series shown in Fig. 6 is based on methods developed in a previous study²³. Instantaneous FRP observations from AHI over southeastern Australia (domain of Fig. 1) were accumulated in hourly intervals. Mean hourly FRP was calculated excluding fire pixels with missing or invalid FRP retrievals. These mean hourly FRP values were multiplied by the hourly total detected fire pixels to give a total hourly FRP. This value was then divided by the number of scenes with detected fire during each hourly interval, yielding a normalized hourly FRP time series.

DATA AVAILABILITY

The CALIOP data that support the findings of this study are available from https://eosweb.larc.nasa.gov/project/calipso/calipso_table. OMPS NM data are available from <https://ozoneaq.gsfc.nasa.gov/data/omps/>. A detailed timeline of ANYSO fire and pyroCb activity is available from the corresponding author upon request, along with derived stratospheric smoke mass estimates.

Imagery products based on AHI data, including the pyroCb detection product, are posted in near-real-time on the Naval Research Laboratory's pyroCb website: <http://www.nrlmry.navy.mil/pyrocb-bin/pyrocb.cgi>. OMPS-NPP LP L2 Aerosol Extinction Vertical Profile swath multi-wavelength daily 3slit Collection 2 V2.0, are accessible from Goddard Earth Sciences Data and Information Services Center, accessed [11/10/2020], <https://doi.org/10.5067/CX2B9NW6FI27>. The standard MODIS fire products (MOD14) can be obtained from https://firms.modaps.eosdis.nasa.gov/active_fire/#firms-shapefile. Data from NOAA's Fire Detection and Characterization Algorithm, which is the ABI implementation of the WFABBA, can be obtained from the NOAA Comprehensive Large Array-data Stewardship System (CLASS) at <https://www.class.noaa.gov> and from the participating members of the Big Data project enumerated here: <https://www.ncdc.noaa.gov/data-access/satellite-data/satellite-data-noaa-big-data-project>.

Australian weather radar data can be obtained in a compressed file format from the NCI server with appropriate date syntax and radar station code. For example, full volume scans from the Captain's Flat location (code 40) on 2019/12/31 can be retrieved here http://dapds00.nci.org.au/thredds/fileServer/rq0/40/2019/vol/40_20191231.pvol.zip. More information about the radar sites can be found here http://www.bom.gov.au/australia/radar/info/nsw_info.shtml#captains-flat40.

Received: 16 January 2021; Accepted: 9 June 2021;

Published online: 13 July 2021

REFERENCES

- Khaykin, S. et al. The 2019/20 Australian wildfires generated a persistent smoke-charged vortex rising up to 35 km altitude. *Commun. Earth Environ.* **1**, 22 (2020).
- Peterson, D. A. et al. Wildfire-driven thunderstorms cause a volcano-like stratospheric injection of smoke. *npj Clim. Atmos. Sci.* **1**, 30 (2018).

3. Burgess, T. Burgmann, J. R. Hall, S. Holmes, D. & Turner, E. Black Summer: Australian newspaper reporting on the nation's worst bushfire season. *Monash Climate Change Communication Research Hub*. p. 30 (Monash University, 2020).
4. Australian Government. *Estimating greenhouse gas emissions from bushfires in Australia's temperate forests: focus on 2019-20*. (Department of Industry, Science, Energy and Resources, 2020).
5. Baars, H. et al. The unprecedented 2017-2018 stratospheric smoke event: decay phase and aerosol properties observed with the EARLINET. *Atmos. Chem. Phys.* **19**, 15183–15198 (2019).
6. Bourassa, A. E. et al. Satellite limb observations of unprecedented forest fire aerosol in the stratosphere. *J. Geophys. Res. Atmos.* **124**, 9510–9519 (2019).
7. Christian, K. et al. Radiative forcing and stratospheric warming of pyrocumulonimbus smoke aerosols: first modeling results with multisensor (EPIC, CALIPSO, AND CATS) views from space. *Geophys. Res. Lett.* **46**, 10061–10071 (2019).
8. Yu, P. et al. Black carbon lofts wildfire smoke high into the stratosphere to form a persistent plume. *Science* **365**, 587–590 (2019).
9. Abatzoglou, J. T., Williams, A. P. & Barbero, R. Global emergence of anthropogenic climate change in fire weather indices. *Geophys. Res. Lett.* **46**, 326–336 (2019).
10. Di Virgilio, G. et al. Climate change increases the potential for extreme wildfires. *Geophys. Res. Lett.* **46**, 8517–8526 (2019).
11. Rosenfeld, D. et al. The Chisholm firestorm: observed microstructure, precipitation and lightning activity of a pyro-cumulonimbus. *Atmos. Chem. Phys.* **7**, 645–659 (2007).
12. Reutter, P. et al. 3-D model simulations of dynamical and microphysical interactions in pyroconvective clouds under idealized conditions. *Atmos. Chem. Phys.* **14**, 7573–7583 (2014).
13. Chang, D. et al. Comprehensive mapping and characteristic regimes of aerosol effects on the formation and evolution of pyro-convective clouds. *Atmos. Chem. Phys.* **15**, 10325–10348 (2015).
14. Kablick, G. et al. The great slave lake PyroCb of 5 August 2014: observations, simulations, comparisons with regular convection, and impact on UTLS water vapor. *J. Geophys. Res. Atmos.* **123**, 12 (2018).
15. Fromm, M., Peterson, D., & Di Girolamo, L. The Primary convective pathway for observed wildfire emissions in the upper troposphere and lower stratosphere: a targeted reinterpretation. *J. Geophys. Res. Atmos.* **124**, 13254–13272 (2019).
16. Clements, C. B. et al. The rapid deployments to wildfires experiment (RaDFIRE) observations from the fire zone. *Bull. Am. Meteorol. Soc.* **99**, 2539–2559 (2018).
17. Rodriguez, B., Lareau, N. P., Kingsmill, D. E. & Clements, C. B. Extreme pyroconvective updrafts during a megafire. *Geophys. Res. Lett.* **47**, e2020GL089001 (2020).
18. Fromm, M. et al. Observations of boreal forest fire smoke in the stratosphere by POAM III, SAGE II, and lidar in 1998. *Geophys. Res. Lett.* **27**, 1407–1410 (2000).
19. Fromm, M. D. & Servranckx, R. Transport of forest fire smoke above the tropopause by supercell convection. *Geophys. Res. Lett.* **30**, 49–52 (2003).
20. Peterson, D. A. et al. Detection and inventory of intense pyroconvection in Western North America using GOES-15 daytime infrared data. *J. Appl. Meteorol. Climatol.* **56**, 471–493 (2017).
21. Peterson, D. A., Hyer, E. J., Campbell, J. R., Solbrig, J. E. & Fromm, M. D. A Conceptual model for development of intense pyrocumulonimbus in Western North America. *Mon. Weather Rev.* **145**, 2235–2255 (2017).
22. Fromm, M. et al. The untold story of pyrocumulonimbus. *Bull. Am. Meteorol. Soc.* **91**, 1193–1209 (2010).
23. Peterson, D. A. et al. The 2013 rim fire implications for predicting extreme fire spread, pyroconvection, and smoke emissions. *Bull. Am. Meteorol. Soc.* **96**, 229–247 (2015).
24. Tory, K. J., Thurston, W. & Kepert, J. D. Thermodynamics of pyrocumulus: a conceptual study. *Mon. Weather Rev.* **146**, 2579–2598 (2018).
25. Tory, K. J. & Kepert, J. D. Pyrocumulonimbus firepower threshold: assessing the atmospheric potential for pyroCb. *Weather Forecasting* **36**, 439–456 (2020).
26. Guan, H. et al. A multi-decadal history of biomass burning plume heights identified using aerosol index measurements. *Atmos. Chem. Phys.* **10**, 6461–6469 (2010).
27. Cruz, M. G. et al. Anatomy of a catastrophic wildfire: the black saturday kilmore east fire in Victoria, Australia. *Ecol. Manag.* **284**, 269–285 (2012).
28. McRae, R. H. D., Sharples, J. J. & Fromm, M. Linking local wildfire dynamics to pyroCb development. *Nat. Hazards Earth Syst. Sci.* **15**, 417–428 (2015).
29. Fromm, M. et al. Stratospheric impact of the Chisholm pyrocumulonimbus eruption: 1. Earth-viewing satellite perspective. *J. Geophys. Res. Atmos.* **113**, e88101 (2008).
30. Kablick, G. P., Allen, D. R., Fromm, M. D. & Nedoluha, G. E. Australian PyroCb Smoke Generates Synoptic-Scale Stratospheric Anticyclones. *Geophys. Res. Lett.* **47**, e2020GL088101 (2020).
31. Allen, D. R., Fromm, M. D., Kablick, G. P. & Nedoluha, G. E. Smoke with induced rotation and lofting (SWIRL) in the stratosphere. *J. Atmos. Sci.* **77**, 4297–4316 (2020).
32. Robock, A., Marquardt, A., Kravitz, B. & Stenchikov, G. Benefits, risks, and costs of stratospheric geoengineering. *Geophys. Res. Lett.* **36**, L19703 (2009).
33. Solomon, S. et al. The persistently variable “background” stratospheric aerosol layer and global climate change. *Science* **333**, 866–870 (2011).
34. Ridley, D. A. et al. Total volcanic stratospheric aerosol optical depths and implications for global climate change. *Geophys. Res. Lett.* **41**, 7763–7769 (2014).
35. McCormick, M. P., Thomason, L. W. & Trepte, C. R. Atmospheric effects of the Mt-pinatubo eruption. *Nature* **373**, 399–404 (1995).
36. Holasek, R. E., Self, S. & Woods, A. W. Satellite observations and interpretation of the 1991 Mount Pinatubo eruption plumes. *J. Geophys. Res. Solid Earth* **101**, 27635–27655 (1996).
37. Robock, A., Oman, L. & Stenchikov, G. L. Nuclear winter revisited with a modern climate model and current nuclear arsenals: still catastrophic consequences. *J. Geophys. Res. Atmos.* **112**, D13107 (2007).
38. Dowdy, A. J., Fromm, M. D. & McCarthy, N. Pyrocumulonimbus lightning and fire ignition on Black Saturday in southeast Australia. *J. Geophys. Res. Atmos.* **122**, 7342–7354 (2017).
39. Fromm, M. et al. Stratospheric impact of the Chisholm pyrocumulonimbus eruption: 2. Vertical profile perspective. *J. Geophys. Res. Atmos.* **113**, D08203 (2008).
40. Potter, B. E. A dynamics based view of atmosphere-fire interactions. *Int. J. Wildland Fire* **11**, 247–255 (2002).
41. McRae, R. H. D. & Sharples, J. J. A process model for forecasting conditions conducive to blow-up fire events. in *MODSIM2013, 20th International Congress on Modelling and Simulation. Modelling and Simulation Society of Australia and New Zealand* (eds. Piantadosi, J., Anderssen, R. S. and Boland, J.), p. 187–192. ISBN: 978-0-9872143-3-1. <https://www.mssanz.org.au/modsim2013/A3/mcrae.pdf> (2013).
42. McRae, R. H. D. & Sharples, J. J. Forecasting conditions conducive to blow-up fire events. in *CAWCR Research Letters, 11. The Centre for Australian Weather and Climate Research* (eds. Sandery, P. A., Richter, H., Tory K. & Day, K. A.), p. 14–19. https://www.cawcr.gov.au/researchletters/CAWCR_Research_Letters_11.pdf (2014).
43. Sharples, J. J. et al. Natural hazards in Australia: extreme bushfire. *Clim. Change* **139**, 85–99 (2016).
44. Perrakis, D. D. B., Eade, G. & Hicks, D. *British Columbia Wildfire Fuel Typing and Fuel Type Layer Description. Natural Resources Canada Canadian Forest Service Pacific Forestry Centre Information Report BC-X-444* (Canadian Forest Service Publications, 2018).
45. Williams, R. J., Gill, A. M. & Bradstock, R. A. *Flammable Australia* (CSIRO, 2012).
46. Smith, J. B. et al. A case study of convectively sourced water vapor observed in the overworld stratosphere over the United States. *J. Geophys. Res. Atmos.* **122**, 9529–9554 (2017).
47. Corfidi, S. F. et al. Revisiting the 3–4 April 1974 super outbreak of tornadoes. *Weather Forecast.* **25**, 465–510 (2010).
48. Knupp, K. R. et al. Meteorological overview of the devastating 27 APRIL 2011 tornado outbreak. *Bull. Am. Meteorol. Soc.* **95**, 1041–1062 (2014).
49. Nimchuk, N. Wildfire behavior associated with upper ridge breakdown. *Alberta Energy and Natural Resources Forest Service Report No. T/50*. Edmonton, Alberta (Alberta Energy and Natural Resources, Forest Service, Edmonton, 1983).
50. Westphal, D. L. & Toon, O. B. Simulations of microphysical, radiative, and dynamic processes in a continental-scale forest-fire smoke plume. *J. Geophys. Res. Atmos.* **96**, 22379–22400 (1991).
51. Saide, P. E. et al. Revealing important nocturnal and day-to-day variations in fire smoke emissions through a multiplatform inversion. *Geophys. Res. Lett.* **42**, 3609–3618 (2015).
52. Giglio, L., Csiszar, I. & Justice, C. O. Global distribution and seasonality of active fires as observed with the Terra and Aqua Moderate Resolution Imaging Spectroradiometer (MODIS) sensors. *J. Geophys. Res. Biogeosci.* **111** (2006).
53. Kirchmeier-Young, M. C., Gillett, N. P., Zwiars, F. W., Cannon, A. J. & Anslow, F. S. Attribution of the Influence of Human-Induced Climate Change on an Extreme Fire Season. *Earths Future* **7**, 2–10 (2019).
54. CAL FIRE. 2020 Fire Season. <https://www.fire.ca.gov/incidents/2020/> (accessed March 2021).
55. National Aeronautics and Space Administration. 2020 Fire Season in the Western U.S. <https://earthobservatory.nasa.gov/images/event/146855/2020-fire-season-in-the-western-us> (accessed March 2021).
56. University of Wisconsin-Madison. Pyrocumulonimbus cloud spawned by the Creek Fire in California. <https://cimss.ssec.wisc.edu/satellite-blog/archives/38199> (accessed February 2021).
57. Winker, D. M. et al. The CALIPSO Mission A Global 3D View of Aerosols and Clouds. *Bull. Am. Meteorol. Soc.* **91**, 1211–1229 (2010).
58. Flynn, L. et al. Performance of the Ozone Mapping and Profiler Suite (OMPS) products. *J. Geophys. Res. Atmos.* **119**, 6181–6195 (2014).
59. Torres, O. et al. Stratospheric Injection of Massive Smoke Plume From Canadian Boreal Fires in 2017 as Seen by DSCOVR-EPIC, CALIOP, and OMPS-LP Observations. *J. Geophys. Res. Atmos.* **125** (2020).

60. Butchart, N. The Brewer-Dobson circulation. *Rev. Geophys.* **52**, 157–184 (2014).
61. Leblanc, T., et al. A 25-Year High in Global Stratospheric Aerosol Loading [in “State of the Climate in 2019”. *Bull. Am. Meteorol. Soc.* **101**, Sidebar 2.2 (2020)].
62. Stocker, M., Ladstaedter, F., Wilhelmssen, H. & Steiner, A. K. Quantifying Stratospheric Temperature Signals and Climate Imprints From Post-2000 Volcanic Eruptions. *Geophys. Res. Lett.* **46** (2019).
63. Kloss, C. et al. Stratospheric aerosol layer perturbation caused by the 2019 Raikoke and Ulawun eruptions and their radiative forcing. *Atmos. Chem. Phys.* **21**, 535–560 (2021).
64. Robock, A. & Zambri, B. Did Smoke From City Fires in World War II Cause Global Cooling? *J. Geophys. Res.: Atmos.* **123**, 10,314–10,325 (2018).
65. LaRoche, K. T. & Lang, T. J. Observations of Ash, Ice, and Lightning within Pyroclastic Clouds Using Polarimetric NEXRAD Radars and the National Lightning Detection Network. *Mon. Weather Rev.* **145**, 4899–4910 (2017).
66. Lareau, N. P., Nauslar, N. J. & Abatzoglou, J. T. The Carr Fire Vortex: A Case of Pyrotornadogenesis? *Geophys. Res. Lett.* **45**, 13107–13115 (2018).
67. McRae, R. & Sharples, J. Assessing mitigation of the risk from extreme wildfires using MODIS hotspot data. in *Proceedings - 21st International Congress on Modelling and Simulation, MODSIM 2015* 250–256 (Modelling and Simulation Society of Australia and New Zealand Inc. (MSSANZ), 2015). <https://doi.org/10.36334/modsim.2015.a4.mcrae>
68. Boer, M. M., de Dios, V. R. & Bradstock, R. A. Unprecedented burn area of Australian mega forest fires. *Nat. Clim. Change* **10**, 171–172 (2020).
69. National Aeronautics and Space Administration and National Oceanic and Atmospheric Administration. FIREX-AQ Investigating smoke from wildfires and biomass burning. <https://csl.noaa.gov/projects/firex-aq/> (accessed January 2021).
70. Bohlmann, S., Baars, H., Radenz, M., Engelmann, R. & Macke, A. Ship-borne aerosol profiling with lidar over the Atlantic Ocean: from pure marine conditions to complex dust-smoke mixtures. *Atmos. Chem. Phys.* **18**, 9661–9679 (2018).
71. Ohneiser, K. et al. Smoke of extreme Australian bushfires observed in the stratosphere over Punta Arenas, Chile, in January 2020: optical thickness, lidar ratios, and depolarization ratios at 355 and 532 nm. *Atmos. Chem. Phys.* **20**, 8003–8015 (2020).
72. Field, R. D. et al. Simulating the Black Saturday 2009 smoke plume with an interactive composition-climate model: Sensitivity to emissions amount, timing, and injection height. *J. Geophys. Res.: Atmos.* **121**, 4296–4316 (2016).
73. Dirksen, R. J. et al. An aerosol boomerang: Rapid around-the-world transport of smoke from the December 2006 Australian forest fires observed from space. *J. Geophys. Res.: Atmos.* **114** (2009).
74. Giglio, L., Schroeder, W. & Justice, C. O. The collection 6 MODIS active fire detection algorithm and fire products. *Remote Sens. Environ.* **178**, 31–41 (2016).
75. García, M. J. L. & Caselles, V. Mapping burns and natural reforestation using thematic Mapper data. *Geocarto Int* **6**, 31–37 (1991).
76. Penman, T. D. & York, A. Climate and recent fire history affect fuel loads in Eucalyptus forests: Implications for fire management in a changing climate. *Ecol. Manag.* **260**, 1791–1797 (2010).
77. Reisen, F., Meyer, C. P., Weston, C. J. & Volkova, L. Ground-Based Field Measurements of PM_{2.5} Emission Factors From Flaming and Smoldering Combustion in Eucalypt Forests. *J. Geophys. Res.: Atmos.* **123**, 8301–8314 (2018).
78. Josephson, A. J., Castano, D., Holmes, M. J. & Linn, R. R. Simulation Comparisons of Particulate Emissions from Fires under Marginal and Critical Conditions. *Atmosphere* **10** (2019).
79. Possell, M. & Bell, T. L. The influence of fuel moisture content on the combustion of Eucalyptus foliage. *Int. J. Wildland Fire* **22**, 343–352 (2013).
80. Taha, G. et al. OMPS LP Version 2.0 Multi-wavelength aerosol extinction coefficient retrieval algorithm. *Atmos. Meas. Tech.* **14**, 1015–1036 (2021).
81. McCarthy, N., Guyot, A., Dowdy, A. & McGowan, H. Wildfire and Weather Radar: A Review. *J. Geophys. Res.: Atmos.* **124**, 266–286 (2019).
82. Wooster, M. J., Roberts, G., Perry, G. L. W. & Kaufman, Y. J. Retrieval of biomass combustion rates and totals from fire radiative power observations: FRP derivation and calibration relationships between biomass consumption and fire radiative energy release. *J. Geophys. Res.: Atmos.* **110**, D24311 (2005).
83. Schroeder, W., Csiszar, I., Giglio, L. & Schmidt, C. C. On the use of fire radiative power, area, and temperature estimates to characterize biomass burning via moderate to coarse spatial resolution remote sensing data in the Brazilian Amazon. *J. Geophys. Res.* **115**, D21121 (2010).
84. Schmidt, C. C., Hoffman, J., Prins, E. & Lindstrom, S. *GOES-R Advanced Baseline Imager (ABI) Algorithm Theoretical Basis Document For Fire/Hot Spot Characterization*. https://www.star.nesdis.noaa.gov/goesr/documents/ATBDs/Baseline/ATBD_GOES-R_FIRE_v2.6_Oct2013.pdf (2013).
85. Schmidt, C. C. Monitoring fires with the GOES-R series. In *The GOES-R series: a new generation of geostationary environmental satellites*. 145–163 (Elsevier, 2020).

ACKNOWLEDGEMENTS

We are grateful to Daniel Lindsey at the National Oceanic and Atmospheric Administration Center for Satellite Applications and Research and the Cooperative Institute for Research in the Atmosphere (CIRA) for providing GeoColor imagery of the stratospheric smoke plumes. We also thank Melinda Surratt at the Naval Research Laboratory for assistance with satellite data processing. We thank the National Computational Infrastructure (NCI Australia) for providing weather radar data. This research was funded in part by the Naval Innovative Science and Engineering (NISE) program at the Naval Research Laboratory and by the U.S. Office of Naval Research. NASA supported this work under the Aura Science Team (NNH19ZDA001N-AURAST; 19-AURAST19-0057) and FIREX-AQ Science Team (80HQTR18T0063). Additional support for D.A.P. was provided by the NASA New Investigator Program (80HQTR18T0073). G.T. was funded by NASA contract 80NSSC18K0847. M.T.D. was funded through NASA contract NNG17HP01C.

AUTHOR CONTRIBUTIONS

D.A.P. assembled each data source, designed the experiments, conducted meteorological analyses, and wrote the narrative. M.D.F. and G.P.K. analyzed radar echo-top data and satellite imagery for observed pyroCb activity and supported all stratospheric aerosol mass calculations. R.H.D.M. provided burned area estimates for all blow-up fires of relevance. M.D.F. and R.H.D.M. supported construction of the ANYSO timeline of fire and pyroCb activity. J.R.C. provided all lidar data and supported each step of the analysis. E.J.H. provided total smoke mass and energy release estimates for relevant fires and supported data interpretation. G.T. provided and analyzed all OMPS LP data, including comparisons between pyroCb and volcanic plumes. C.P.C. produced imagery and supported analysis of all AHI data used in this study. C.C.S. applied the WFABBA algorithm to retrieve FRP data from AHI and supported subsequent analysis. M.T.D. provided and analyzed UVAI data from OMPS NM.

COMPETING INTERESTS

The authors declare no competing interests.

ADDITIONAL INFORMATION

Supplementary information The online version contains supplementary material available at <https://doi.org/10.1038/s41612-021-00192-9>.

Correspondence and requests for materials should be addressed to D.A.P.

Reprints and permission information is available at <http://www.nature.com/reprints>

Publisher's note Springer Nature remains neutral with regard to jurisdictional claims in published maps and institutional affiliations.



Open Access This article is licensed under a Creative Commons Attribution 4.0 International License, which permits use, sharing, adaptation, distribution and reproduction in any medium or format, as long as you give appropriate credit to the original author(s) and the source, provide a link to the Creative Commons license, and indicate if changes were made. The images or other third party material in this article are included in the article's Creative Commons license, unless indicated otherwise in a credit line to the material. If material is not included in the article's Creative Commons license and your intended use is not permitted by statutory regulation or exceeds the permitted use, you will need to obtain permission directly from the copyright holder. To view a copy of this license, visit <http://creativecommons.org/licenses/by/4.0/>.

This is a U.S. Government work and not under copyright protection in the US; foreign copyright protection may apply 2021